

Synthesis and Advanced Electrochemical Characterization of Multifunctional Electrocatalytic Composite for Unitized Regenerative Fuel Cell

Léonard Jean Moriau,^{†,‡} Marjan Bele,^{*,§} Alen Vižintin,[§] Francisco Ruiz-Zepeda,^{§,||} Urša Petek,[§] Primož Jovanovič,[†] Martin Sala,[⊥] Miran Gabersček,[§] and Nejc Hodnik^{*,†,‡,§}

[†]Department of Catalysis and Chemical Reaction Engineering, National Institute of Chemistry, Hajdrihova 19, SI-1000 Ljubljana, Slovenia

[‡]Jozef Stefan International Postgraduate School, Jamova 39, SI-1000, Ljubljana, Slovenia

[§]Department of Materials Chemistry, National Institute of Chemistry, Hajdrihova 19, SI-1000 Ljubljana, Slovenia

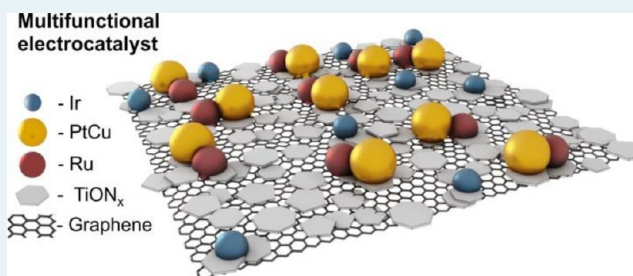
^{||}Department of Physics and Chemistry of Materials, Institute of Metals and Technology, Lepi pot 11, SI-1000 Ljubljana, Slovenia

[⊥]Department of Analytical Chemistry, National Institute of Chemistry, Hajdrihova 19, SI-1000 Ljubljana, Slovenia

Supporting Information

ABSTRACT: A multifunctional electrocatalytic composite was synthesized for use as a generic catalytic material in the polymer electrolyte membrane (PEM) type reactors, working in either fuel cell, direct methanol fuel cell, or electrolyzer mode. It is constructed from graphene sheets evenly covered with TiON_x on which PtCu, Ir, and Ru nanoparticles are immobilized. It enables high performances for oxygen reduction, hydrogen and methanol oxidation, and also hydrogen and oxygen evolution. Its activity is either higher or comparable to the monofunctional benchmark catalysts, namely, Pt, PtRu, and Ir nanoparticles. An important part of this study is the advanced electrochemical degradation investigation. With the use of an electrochemical flow cell coupled to ICP-MS and combining these results with identical location electron microscopy, we reveal not only potential shortcomings but also opportunities for our material. As a result, we also put forward general guidelines for the appropriate use of multifunctional electrocatalysts.

KEYWORDS: electrocatalysis, bifunctional electrocatalysts, oxygen evolution reaction, oxygen reduction reaction, IL-TEM, IL-SEM, EFC-ICP-MS



1. INTRODUCTION

Electrochemistry is an important part of society and industry with multiple applications, and in recent decades, the field has grown with the increasing interest in new storage and conversion devices such as batteries, fuel cells, and electrolyzers.^{1–5} The major challenge is to switch from fossil fuels to sun-based sustainable energy. Because of the intermittency of these renewable energy sources, either from wind farms or solar panels, effective energy storage and efficient conversion processes must be developed and optimized.^{6,7} An electrolyzer is a practical way to split water into hydrogen and oxygen when there is a surplus of energy. By contrast, a fuel cell converts this chemically stored energy (as hydrogen) back to electricity, heat, and water. The unitized regenerative (or reversible) fuel cell (URFC) presents a fundamentally interesting and practical way to do both in one device. Indeed, an URFC can operate in two different modes: the fuel cell mode, where electrical energy is produced; and the electrolyzer mode, where water is split.^{8–10} However, in addition to the same issues that are

present in monofunctional catalyst devices (fuel cell and electrolyzer), namely, sluggish oxygen reduction (ORR) and oxygen evolution (OER) reactions, respectively, URFC catalysts suffer also from significant stability problems.^{7,8,11} Thus, there is a great need for fundamental and applied studies on an efficient bifunctional catalyst for both oxygen-involved reactions.¹² The straightforward approaches to obtain a bifunctional catalyst are (i) physical mixing of Pt and Ir oxide catalysts,^{13–15} (ii) deposition of Pt on Ir or Ir-oxide^{16–22} and (iii) deposition of Ir/Ir-oxide on Pt.^{23–26} However, since Pt and Ir are rare, scarce, and expensive materials,²⁷ their (i) utilization and (ii) performance has to be optimized. The first point can be addressed by dispersing noble metals in the form of nanoparticles on high-surface-area electrically conductive support.^{28,29} In addition to the effective dispersion, a synergy

Received: August 8, 2019

Revised: October 8, 2019

Published: October 30, 2019

effect could be expected, for example, the strong metal–support interaction (SMSI).^{30,31} Some groups have obtained promising results for OER with a carbon support.^{32–34} However, we note that the use of carbon is not recommended as it is neither thermodynamically nor kinetically stable at acidic OER conditions when in contact with noble metal catalytic nanoparticles.³⁵ Carbon is usually used in a composite with Pt nanoparticles for ORR where stability becomes a serious issue at elevated temperatures.^{36,37} Other supports have also been investigated, for instance, carbides³⁸ or oxides;^{39,40} however, they still have not reached a commercial level. Recently, TiO₂ was presented as a stable and high-surface-area support for IrO₂ during OER.⁴¹ However, as TiO₂ is semiconductive, high loading of Ir was necessary to obtain a sufficient electrical conductivity. This support was also used for a Pt-based ORR catalyst.^{42,43} To address the conductivity issue, one could use a high surface area titanium oxynitride (TiON_x) support.^{44,45} Second, it is known that Pt alloys are currently the most active ORR catalyst^{6,46} and that IrO_x or IrRuO_x present the state-of-the-art OER catalysts.^{6,47,48} Therefore, there is still much room for improvement of the noble metal utilization and performance compared with the state-of-the-art Pt–Ir powder URFC bifunctional catalyst.^{17,22}

Furthermore, an ideal URFC device would not be limited to the oxygen reduction and evolution reactions but could run multiple reactions. The most practical way would be to have one material that could catalyze the most frequent low-temperature fuel cell and electrolyzer reactions. This way, the production of membrane electrode assemblies (MEA) would become straightforward as the same catalyst would be used to produce a cathode and an anode. Multifunctionality of the materials would be shown by also catalyzing other reactions besides ORR and OER, which are hydrogen and methanol oxidation (HOR, MOR) and hydrogen evolution reaction (HER). While hydrogen oxidation and evolution rely on Pt,⁴⁹ methanol oxidation requires the presence of Ru.⁵⁰ In this study, we present the synthesis and advanced electrochemical characterization of multifunctional nanocomposite materials that effectively catalyze all of the mentioned reactions. Importantly, we also provide an advanced in-depth stability study that reveals the shortcomings and opportunities for multifunctional type electrocatalysts.

2. EXPERIMENTAL METHODS

Synthesis. A three-step synthesis was developed in order to obtain the present multifunctional catalyst with nanoparticles of different metals. The full synthesis method can be found in the SI. Briefly, in the first step, TiO₂ nanoparticles embedded in graphene oxide were prepared by mixing Ti isopropoxide (Aldrich, 97%) with some graphene oxide (modified from Marcano's synthesis,⁵¹ see procedure in SI) in a propanol-water (70/30) solvent (Honeywell, 99.8% - Milli-Q water 18.2 MΩ·cm). The mixture is then annealed at 800 °C for 6 h in NH₃ atmosphere to obtain TiON_x embedded on graphene.

The second step of the synthesis is the addition of Pt (Pt(NH₃)₄(NO₃)₂, Alfa Aesar), Cu (Cu(NO₃)₂·3H₂O, Sigma-Aldrich, 98%), and Ru (RuCl₃·H₂O, Apollo Scientific) to the support in a molar ratio of 0.4:1:0.4, respectively. The catalyst was annealed at 800 °C in NH₃ for 1 h. The addition of Pt and Ru precursors during the same annealing step was necessary to obtain nanoparticles of Pt-alloy and Ru next to each other.

The final step is the addition of Ir (IrBr₃·H₂O, Alfa Aesar minimum 35.9% of Ir) with the previously obtained composite

and the thermal treatment of this new mixture at 450 °C in NH₃ for 1 h. The addition of Ir precursor in a third separated step helped to obtain smaller nanoparticles not alloyed with any other metals.

X-ray Diffraction (XRD). XRD studies were carried out with a Siemens D5000 instrument with a Cu Kα1 radiation ($\lambda = 1.5406 \text{ \AA}$) in the 2θ range from 10° (20°) to 60° (90°) with the 0.04° step per 1 s. Samples were prepared on zero-background Si holder. The software X'pert HighScore plus was used to analyze the spectrum.

Electrochemical Characterization. The electrochemical properties of the material were analyzed in a two-compartment electrochemical cell with a conventional three-electrode system controlled by a potentiostat (Potentiostat ECI-200, Nordic electrochemistry). Ag/AgCl was used as a reference and a Pt wire as a counter electrode. However, during degradation studies, a graphite rod was used as the counter electrode to avoid any dissolution and redeposition of Pt on the catalyst. The working electrode was a glassy carbon with an area of 0.196 cm² embedded in PTFE(Pine). To avoid any Cl⁻ ion contamination, the reference electrode was separated from the rest of the cell. Prior to each experiment, the electrochemical cell was boiled in Milli-Q water (18.2 MΩ·cm). All the potentials are given versus the reversible hydrogen electrode (RHE) which was determined in an H₂-saturated environment for each experiment. Every measurement was *iR* corrected. The resistance of the electrolyte was recorded by impedance spectroscopy as described in ref 52. The catalyst ink was prepared by mixing 1 mg of catalyst in 1 mL of Milli-Q water. A droplet of 20 μL (20 μg of catalyst) was dropped on the working electrode after ultrasonication to ensure the homogeneity of the suspension. After the suspension was dried, 5 μL of Nafion:isopropanol solution (1:50) was added on top of the catalyst layer to stabilize the film. The activity for oxygen reduction was tested in 0.1 M HClO₄ (Merck, Suprapur, 70%) electrolyte under O₂ saturated atmosphere between 0.05 and 1 V vs RHE at 20 mV s⁻¹ and 1600 revolutions per minute (rpm). The rotation rate and the scanning speed were kept constant for all activity investigation. The potential window and the gas atmosphere were changed appropriately to the reaction studied. Afterward, the activity for oxygen evolution was investigated between 0.05 and 1.6 V vs RHE in deoxygenated 0.1 M HClO₄. New films were used to study hydrogen evolution, from 0.1 to 0.6 V vs RHE under H₂, and methanol oxidation, from 0.2 to 1.2 V vs RHE in 0.1 M HClO₄ and 1 M CH₃OH (J.T.Baker) electrolyte. Prior to activity measurements, the catalyst was electrochemically activated for 200 cycles between 0.05 and 1.2 V vs RHE at 300 mV s⁻¹ under Ar. During activation, Cu leaches out of the PtCu particles^{53–55} improving the activity for ORR compared to pure Pt. After activity measurements, the materials were degraded for 10 000 cycles within variable potential windows (0.4 to 1.0 V vs RHE for “ORR degradation”, 1.0 to 1.2 V vs RHE for “OER degradation” and 0.4 to 1.6 V vs RHE for “ORR & OER or ALL degradation”) under Ar at 1 V s⁻¹. The thin film on the electrode was dispersed in 0.5 mL of isopropanol in an ultrasound bath for 5 s and later dropped on a TEM grid for ex situ measurement. The anodic scan is shown for all the electrochemical experiments.

Electrochemical Flow Cell–Inductively Coupled Plasma–Mass Spectrometry. An electrochemical flow cell (EFC) was coupled with an ICP-MS detector, namely Agilent 7500ce ICP-MS instrument (Agilent Technologies, Palo Alto,

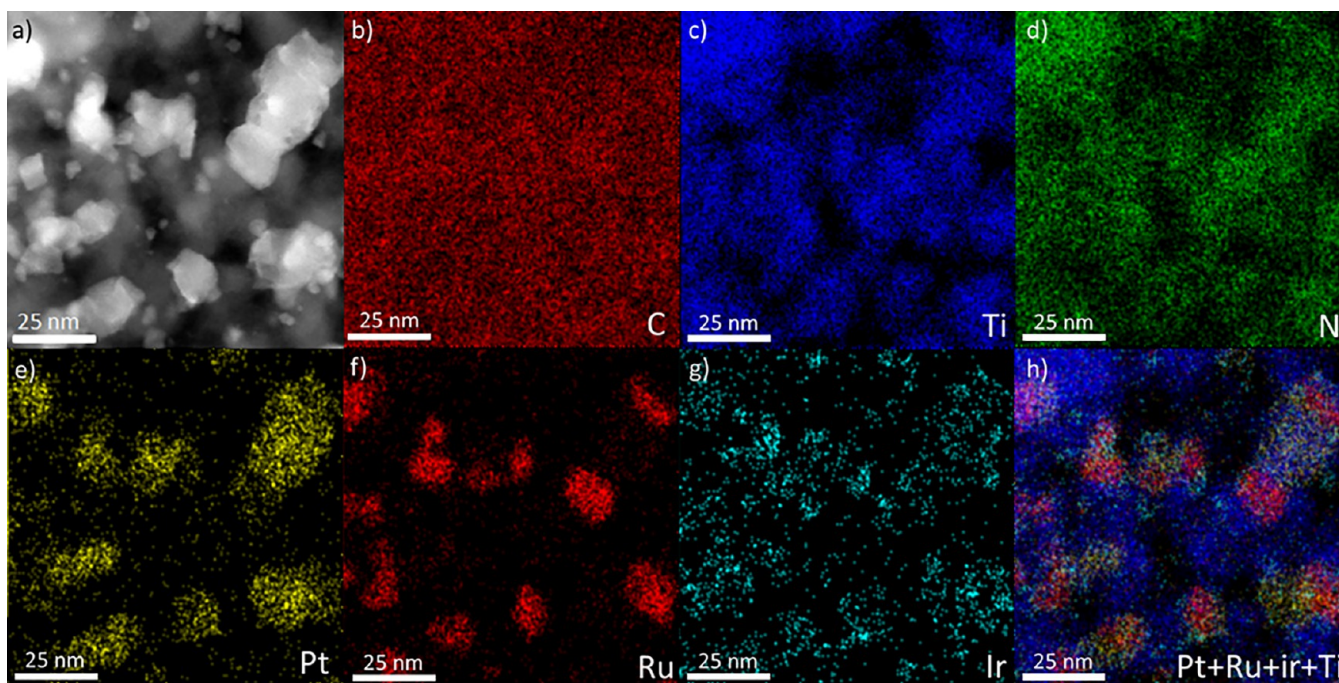


Figure 1. (a) STEM ADF image. (b) EDX mapping of carbon (red), (c) titanium (purple), (d) nitrogen (green), (e) platinum (yellow), (f) ruthenium (red), (g) iridium (blue), and (h) overlay of platinum, ruthenium, iridium, and titanium from the composite TiON-RuPtCu-Ir.

CA), equipped with a MicroMist glass concentric nebulizer and a Peltier cooled Scott-type double-pass quartz spray chamber. A forward radio frequency power of 1500 W was used with Ar gas flows: carrier, 0.85 L min⁻¹; makeup, 0.28 L min⁻¹; plasma, 1 L min⁻¹; and cooling, 15 L min⁻¹. Signals of the five metals (Ti, Cu, Ru, Ir, and Pt) were recorded. In order to convert the measured ICP-MS signal from EC experiments (number of counts) to concentration (ppb), seven standard solutions were measured: 1, 2, 5, 10, 20, 50, and 100 ppb of each metal. The EFC was custom-made of PEEK housing. The design mimicked that of a commercial cross-flow metallic cell (cross-flow cell, BASi). The working and counter electrode were glassy carbon discs (3 mm diameter) embedded into PEEK material (ALS dual type electrode for cross-flow cell, 25 × 25 mm). The inlet of the electrolyte flow was at the counter electrode and the outlet leading to the ICP-MS detector was at the working electrode side. The reference electrode (Ag/AgCl, MW-2030, BASi) was placed into the reference retainer that was connected to the main cell compartment through a small hole, with the opening centered between the working and counter electrode. The potential of the reference electrode was determined prior to flow experiments in a separate cell setup versus RHE. The volume of the main cell compartment was established with a homemade silicon gasket that was 1.0 mm thick and had an oval-shaped opening of 1.5 cm². The electrolyte (0.1 M HClO₄) was pumped through the cell at a constant flow of 400 μL min⁻¹. Initially, Milli-Q water was pumped through the cell and switched to 0.1 M HClO₄ solution cca. 10 min prior to electrochemical experiments in order to record dissolution of metals into acid at open-circuit potential (OCP). A diagonal 4-way flow valve (V-100D, Idex, from PEEK) was used to switch the flow from water to acid, and two syringe pumps (sp100i, WPI and 11 plus, Harvard Apparatus) were used to pump both liquids at constant flow to ensure immediate transition without notable flow or pressure changes. Electrochemical control of the cell was established

with a BioLogic SP-300 potentiostat, equipped with an analog ramp generator. The electrochemical experiments included an electrochemical activation protocol (cyclic voltammetry, scan rate 300 mV s⁻¹, potential range 0.05 to 1.2 V, 200 cycles) and subsequent slow potential cycling (analog cyclic voltammetry, scan rate 20 mV s⁻¹) in varying potential ranges. Five potential cycles were repeated in each range. The start of the first cycle and the end of the fifth cycle was at OCP. The potential limits of the intermediate cycles were as follows: 0.4 to 1.0 V vs RHE; 1.2 to 1.6 V vs RHE; 0.4 to 1.6 V vs RHE; 0.0 to 1.6 V vs RHE and -0.1 to 1.0 V vs RHE. Between each set of five potential cycles, 3 min of OCP were implemented. The experiments were performed in a standard three-electrode setup, with 100 μV voltage resolution, 1 mA current range, and 160 kHz bandwidth. No ohmic drop compensation method was used as the currents were relatively low due to slow potentials sweeps.

Scanning Electron Microscopy and Energy Dispersion X-ray Spectrometry. Scanning electron microscopy (SEM) was carried out using a Zeiss Supra TM 35 VP microscope equipped with an energy dispersive X-ray spectrometer (EDX, Oxford Instruments, Model Inca 400). The operational voltage was set to 7 kV, and the distance between the gun and the sample is 4.5 mm. Three areas were analyzed for statistical relevance. In order to perform identical location - SEM (IL-SEM), 5 μL of the catalyst ink was deposited on a carbon rod as a working electrode.

Transmission Electron Microscopy and Energy Dispersion X-ray Spectrometry. In order to investigate the modifications undergone in the catalyst during activation, activity measurement and degradation, (identical location) transmission electron microscopy (IL-) TEM, and EDX were carried out using a Cs-corrected microscope CF-ARM Jeol 200 equipped with a SSD Jeol EDX spectrometer. The operational voltage employed was 200 kV. The catalyst suspension was sonicated for 15 min and then diluted 10 times (100 μL of suspension with 900 μL of Milli-Q water). One drop (5 μL) of

the new, diluted suspension was dropped on a TEM gold grid after 5 additional minutes of sonication. The grid was inspected under TEM (“as prepared” sample) before any experiment. After the inspection, the grid was mounted on a glassy carbon disc embedded in Teflon. The same setup as for the electrochemical measurements was used. The Au-grid was rinsed with Milli-Q water, dried and examined by TEM after each step, namely, activation, activity, and degradation.

3. RESULTS AND DISCUSSION

a. Physical Characterization. Synthesis. As-synthesized titanium oxynitride (TiON_x) on graphene shows characteristic diffractions (see Figure S1a and additional information in SI). A detailed analysis showed that pure TiON_x phase without the presence of TiO_2 phase was obtained. After the addition of Ru, Pt, Cu, and Ir, all characteristic peaks appear relatively wide—implying the presence of small nanoparticles (Figure S1b and S2).

Our goal was to cover the micrometer-sized graphene flakes with a layer of TiON_x in order to physically separate the catalytic nanoparticles from the carbon support and thus prevent carbon corrosion during electrochemical operation. Ideally, all of the carbon would be covered with a layer of TiON_x . The actual coverage was investigated using a Scanning (S)TEM-EDX mapping. As can be seen in Figure S3, the titanium EDX signal is superimposed with O and N signals. This confirms that the coverage of TiON_x is close to ideal. This was more or less expected as Ti and graphene have a strong interaction.^{56,57} The overlapping chemical mapping image of the titanium and different metals confirms that there is almost no direct contact between catalytic metals and carbon (Figure 1).

The catalytic nanoparticles exhibit different shapes and sizes depending on their nature (Figures 1a and 2). Three kinds of

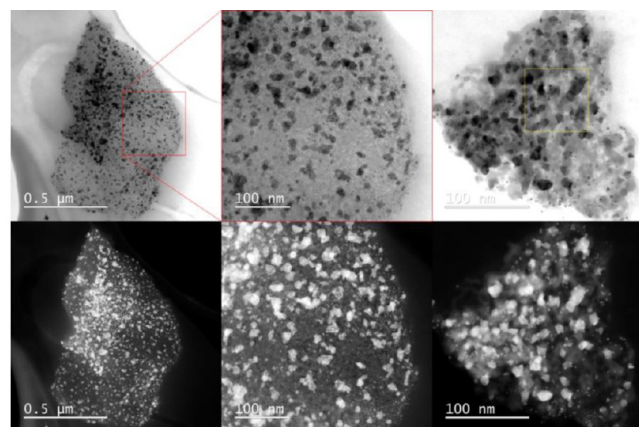


Figure 2. STEM bright-field (BF) and annular dark field (ADF) images of micrometer-sized graphene flakes covered with TiON_x and decorated with PtCu, Ru, and Ir nanoparticles. The yellow square marks the location of EDX maps in Figure 1a).

particles can be distinguished, and interestingly, none are spherical. First, the small irregularly shaped particles (around 5 nm) are pure iridium. The absence of mixing with other metals is in accordance with the phase diagrams.⁵⁸ The small sizes can be explained by the intimate interaction with Ti-based support, known from dimensionally stable anodes,⁵⁹ and the fact that Ir was deposited separately in the last and separate step of the synthesis. Among the bigger particles (above 10 nm), some are

irregularly shaped and exhibit porosity while some have a round shape and do not exhibit visible porosity. The latter were identified as pure Ru, as demonstrated in Figures 2 and S4. As regards the irregular and porous ones, the chemical mapping indicates an alloy between Pt and Cu, as seen in Figure S4. Given the present temperature range of synthesis, the formation of a PtCu alloy is expected and in accordance with a previous synthesis of PtCu-based nanoparticles on carbon.⁶⁰ Interestingly, no alloying between Ru and PtCu is detected. This can also be expected from the phase diagrams and was already observed in our previous study, where Ru did not alloy with Pt or Cu even at the temperature of 800 °C.⁶¹ Interestingly, Ru particles are still in direct physical contact with PtCu particles,⁶² which is important for the methanol oxidation reaction, as explained in continuation.

The exact amount of each metal in the catalyst was obtained by ICP-MS, and the results are presented in Table 1. Altogether, the precious metals represent only approximately one-fifth of the total mass of the catalyst.

Table 1. Weight and Atomic Percent of Catalytic Metals As Determined by ICP-MS in TiON_x -RuPtCu-Ir

elements	weight (%)	atomic %	ratio (atomic)
Cu	6.74	1.06	2.5
Pt	7.68	0.39	0.925
Ru	2.81	0.28	0.65
Ir	3.5	0.18	0.425
total	20.73	1.91	

b. Electrochemical Characterization. An overview of the electrochemical activity for oxygen reduction and oxygen evolution, as the most relevant URFC reactions, is shown in Figure 3a. The cyclic voltammograms (CV) were recorded in oxygen saturated 0.1 M HClO_4 solution in the potential range from 0.4 to 1.6 V vs RHE. For comparison purposes, the CVs of Ir-black and Pt/C are also included. It should be noted that the real electrochemical surface area (ECSA) of the present catalysts was not undoubtedly determined. Indeed, the usual methods such as CO-stripping or HUPD are either not applicable or have a limited reliability in the case of Ir-based metal oxide.⁶³ The only effective technique seems to be the highly toxic mercury underpotential deposition. BET measurements, on the other hand, are not relevant in the case of a supported catalyst. Still, one can carry out normalization by mass of precious metals, which provides rough information about potential industrial relevance of a catalyst.

For both reactions, the onset potentials are comparable to the benchmarks, Pt (Tanaka) and Ir black for ORR and OER, respectively. However, we must note that the amount of precious metal in the present bifunctional catalyst is 1 order of magnitude smaller than in the benchmarks. Therefore, the mass activity is also 1 order of magnitude greater than for both Pt/C (ORR) and Ir black (OER) (see Supporting Information for mass-normalized graphs, Figures S5 and S6). Exact performance data are listed in Table 2. The common way to evaluate an ORR catalyst is to extract the mass-transport-corrected (Koutecký–Levich equation) current density at 0.9 V.⁶⁴ The mass-normalized current density of the present multifunctional electrocatalytic composite is almost 3 times higher than that of the benchmarks. For OER typically the current density at 1.55 V vs RHE is taken for activity comparisons. At this potential, the current density of the

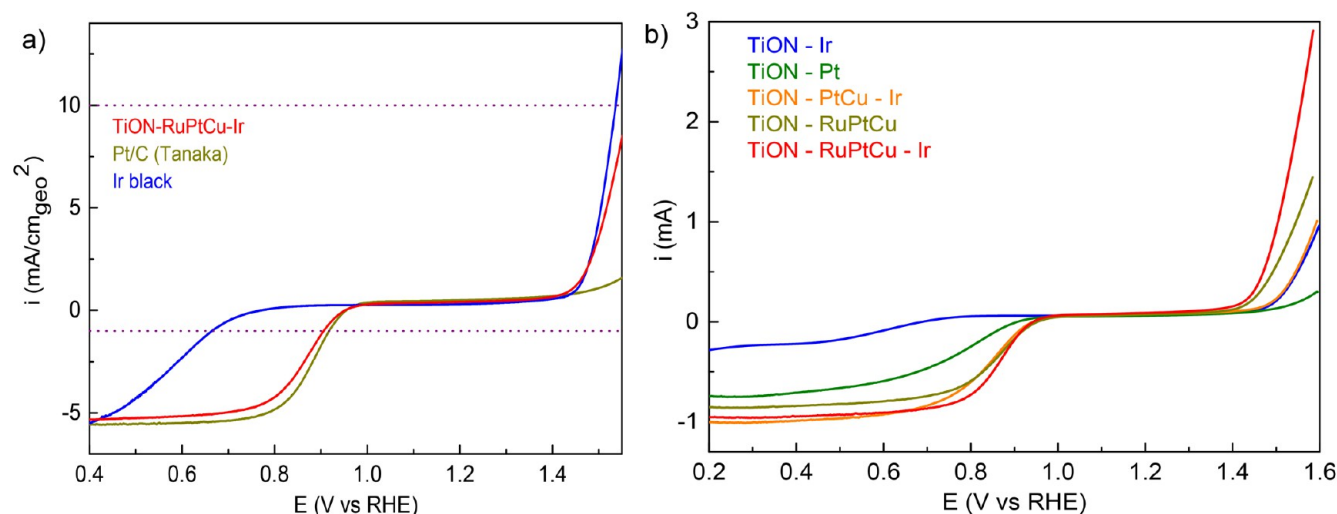


Figure 3. (a) Comparison of our catalyst with the benchmarks for ORR and OER. Two violet vertical lines indicate the current densities where activity can be extracted. (b) Comparison between different Graphene/TiON_x-based catalysts loaded with different metals for oxygen reduction and oxygen evolution reactions. The polarization curves were recorded at 20 mV s⁻¹, in 0.1 M HClO₄, 1600 rpm, under O₂ atmosphere.

Table 2. Performance of Our Catalyst, Monofunctional Benchmarks Catalysts for ORR and OER and Bifunctional Catalysts from Literature

	ORR at 0.85 V ^a or 0.9 V vs RHE		OER at 1.55 V vs RHE		ORR at 1 mA cm ⁻²	OER at 10 mA cm ⁻²	ΔE
	j /mA cm ⁻²	j_m /mA mg _{Pt} ⁻¹ or mg _{PtCu} ⁻¹	j /mA cm ⁻²	j_m /mA mg _{Ir} ⁻¹ or mg _{IrRu} ⁻¹	E /V vs RHE	E /V vs RHE	
Pt/C	1.710	36.03	1.591	n.d.	0.917	n.d.	
Ir black	0.2401	n.d.	12.711	124.56	0.665	1.537	
TiON-RuPtCu-Ir	1.348	91.61 (20.1 ^a)	8.586	1333.27	0.911	1.563	0.651
Pt/IrO ₂ ²⁰		15.1 ^a		142.5 ^b			
Pt-Ir/IrO ₂ -PtO ₂ ²⁰		27.4 ^a		207.3 ^b			
Pt/IrO ₂ ²¹		7.1		34.8			
Pt/IrO _x 1:9 ²²		10.1 ^a		58.9			
Pt/IrO _x 3:7 ²²		8.8 ^a		58.5			
Pt/IrO _x 1:1 ²²		7.5 ^a		61.3			
Pt/IrO _x ¹⁶		9.8 ^a		60.4	0.86	1.54	0.68 ^c
Pt/IrO ₂ ¹⁶		35.1 ^a		24.5	0.9	1.58	0.68 ^c
Pt/IrO ₂ 1:9 ¹⁷		107.4 ^a		25.0	0.87	1.56	0.69 ^c
Pt/IrO ₂ 3:7 ¹⁷		44.7 ^a		20.3	0.89	1.575	0.685 ^c
Pt/IrO ₂ 1:1 ¹⁷		35.7 ^a		18.8	0.9	1.585	0.685 ^c
Pt-Ir/rGO_P600 ³³					0.89	1.58	0.69 ^c
Pt-Ir/TiC ³⁸		164		18.4	0.955	1.635	0.68 ^c
PtIr/Ti ₄ O ₇ ⁴⁰					0.905	1.63	0.725 ^c
Pt ₉₀ Ir ₁₀ /TiO ₂ ⁴²					0.856	1.54	0.684 ^c
Pt ₈₀ Ir ₂₀ /TiO ₂ ⁴²					0.848	1.55	0.702 ^c
Pt ₇₀ Ir ₃₀ /TiO ₂ ⁴²					0.836	1.59	0.754 ^c

^aValues obtained at 0.85 V vs RHE. ^bValues obtained at 1.6 V vs RHE. ^cValues extracted from graphs.

bifunctional catalyst reaches 1333 mA mg_{IrRu}⁻¹. This is 10 times higher than the corresponding current density of Ir black. In comparison with the usual mixed of Pt and Ir used as state-of-the-art catalyst, our material also presents good activity with the same order of magnitude for ORR current density and 2 orders of magnitude improvement of OER current density, which is likely due to the presence of Ru. It should be noted that ORR performance for the bifunctional catalysts are evaluated at 0.85 V vs RHE and not 0.9 V due to the usual poorer performance compared to monofunctional catalyst. An alternative methodology for estimation of OER activity has been suggested, namely the potential at which the current density reaches the value of 10 mA cm_{geo}⁻².⁶⁵ This method is

frequently used in the evaluation of bifunctional catalysts. The difference between the potential at which ORR reaches 1 mA cm_{geo}⁻² and the potential where the current reaches 10 mA cm_{geo}⁻² for OER (violet vertical lines in Figure 3a), ΔE, can be taken as a measure of the performance quality of a bifunctional catalyst.^{66,67} As expected, Pt/C and Ir black show poor bifunctional performance. Ir black has a ΔE of 0.872 V while a current of 10 mA cm⁻² was not reached at 1.6 V vs RHE for Pt/C. The overpotential difference of the present multifunctional catalyst is 0.651 V, which is better than the values obtained for mixed Pt/Ir catalysts, which are between 0.67 to over 0.75 V as seen in Table 2.

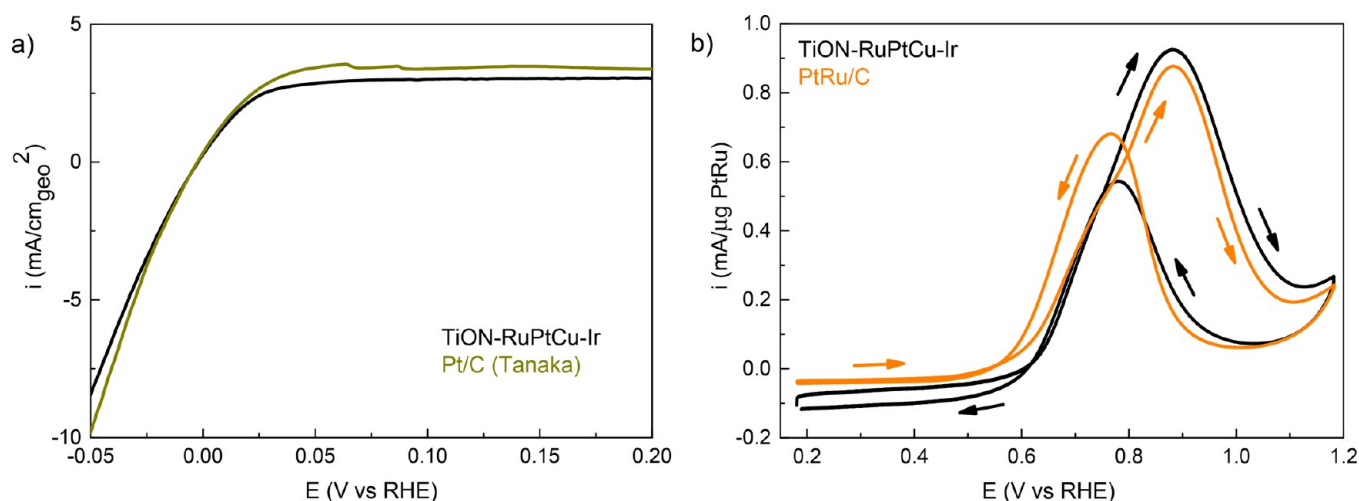


Figure 4. (a) HOR/HER polarization curve at 20 mV s^{-1} , in 0.1 M HClO_4 , 1600 rpm, under H_2 atmosphere. (b) MOR polarization curve in $1 \text{ M CH}_3\text{OH} + 0.1 \text{ M HClO}_4$, 1600 rpm, and a scan rate of 20 mV s^{-1} .

To understand the interplay and the potential benefits of each metal, different variations of catalysts were synthesized using the same TiON_x support as in the case of TiON_x -RuPtCu-Ir. The synthesis was adapted to the selected combinations of metals. TiON_x with Pt, Ir, PtCuIr, or RuPtCu were obtained. A comparison with our bifunctional catalyst can be seen in Figure 3b. One should keep in mind that these catalysts have not been optimized, so their maximum activities could be higher than shown in this work. For the case of ORR, the catalysts with PtCu present a superior activity compared to pure Pt or Ir. The effect of alloying Pt to improve the ORR activity is well-known and has been extensively reported in our previous studies.^{53–55} Analyzing the results of Figure 3b, one finds that the best performance is achieved by the TiON_x -RuPtCu-Ir, both for ORR and ORR. Looking separately at OER, one finds that the presence of Ru has a clear beneficial impact on activity. The better activity of Ru over Ir for OER was already shown before.⁶⁸ The catalyst with both Ir and Ru exhibits a better OER activity than if only one of the metals is added (Figure 3b). It seems that a beneficial interplay occurs when both metals are used simultaneously, similarly, as shown previously for the Ru-PtCu OER catalyst.⁶⁹

Platinum group metal-based nanoparticles are known to be the catalysts of choice for different electrochemical reactions. Specifically, Pt is known to be a good catalyst for ORR and Ir for OER. Along these lines, we expected that the present multicomponent (RuPtCu-Ir) catalyst would not be limited to these two reactions only. Accordingly, we also tested it for the hydrogen-involved reactions (HOR and HER). It is known that these reactions are efficiently catalyzed already by a low amount of Pt. Therefore, it is not surprising that, at low current densities, the activity of the present catalyst is comparable to the activity of the industrial benchmark,^{8,70} as seen in Figure 4a. However, we note again that the Pt loading of our catalyst is merely 7.68%—compared with almost 50% in the benchmark, at the same catalyst loading on the RDE.

The second reaction investigated was the methanol oxidation reaction (MOR), which is utilized at the anode of a direct methanol fuel cell (DMFC). A combination of Pt and Ru (alloyed or unalloyed) is usually a catalyst of choice for MOR. The reason why both elements are needed is the Langmuir–Hilshenwood mechanism of MOR where active

sites for both OH formation (Ru) and also for oxidation of methanol to CO are needed (Pt).⁷¹ It was shown by our group that a catalyst with PtCu alloy with the addition of Ru showed an excellent activity for MOR.^{62,72} As demonstrated in Figure 4b, the performance of the present multicomponent catalyst is comparable to that of the PtRu benchmark (note that in this case, the comparison to pure Pt catalyst is not relevant).

c. Stability Studies. *c.1. Protocols.* The electrochemical stability of the present multicomponent and multifunctional TiON_x -RuPtCu-Ir catalyst studied under different conditions and using different electrochemical techniques such as RDE, IL-SEM, IL-STEM, and EFC-ICP-MS. In terms of corrosion, the EFC-ICP-MS setup is highly sensitive and thus capable of providing extremely accurate potential- and time-resolved dissolution profiles.⁷³ Five different protocols were used to cover the wide URFC operation potential window of the present multifunctional catalyst. Three of the protocols covered the oxygen-involving reactions, namely ORR (0.4 to 1.0 V vs RHE), OER (1.2 to 1.6 V vs RHE), and both ORR & OER (0.4 to 1.6 V vs RHE). The first two protocols simulate the evaluation of ORR and OER in URFC while the third (ORR & OER) simulates the switch from FC mode to WE mode. Indeed, during MEA durability, a constant current of 0.5 A/cm^2 is chosen for FC mode and WE mode, which is usually reached at 0.7 and 1.6 V vs RHE, respectively.^{15,19,32} An additional protocol was used to investigate the effect of a wide potential window during ORR & OER (0.4 to 1.6 V vs RHE). The last protocol examined the stability at the reductive potentials simulating HER conditions (-0.1 to 1.0 V vs RHE). Further discussion about protocol setups is provided in the Supporting Information. In addition to the protocols investigating the potential windows of the studied reactions, the metal dissolution was also measured during the initial 200 activation cycles. All protocols except the activation (200 cycles at 300 mV s^{-1}), involved 5 cycles at 20 mV s^{-1} in order to obtain time- and potential-resolved dissolution profiles which allowed for significant insight into the ongoing degradation mechanisms. The full protocol is shown in Figure S7. In parallel to the ICP-MS results, the electrochemical activities before and after 10 000 cycles in the different potential windows for oxygen-involving reactions were

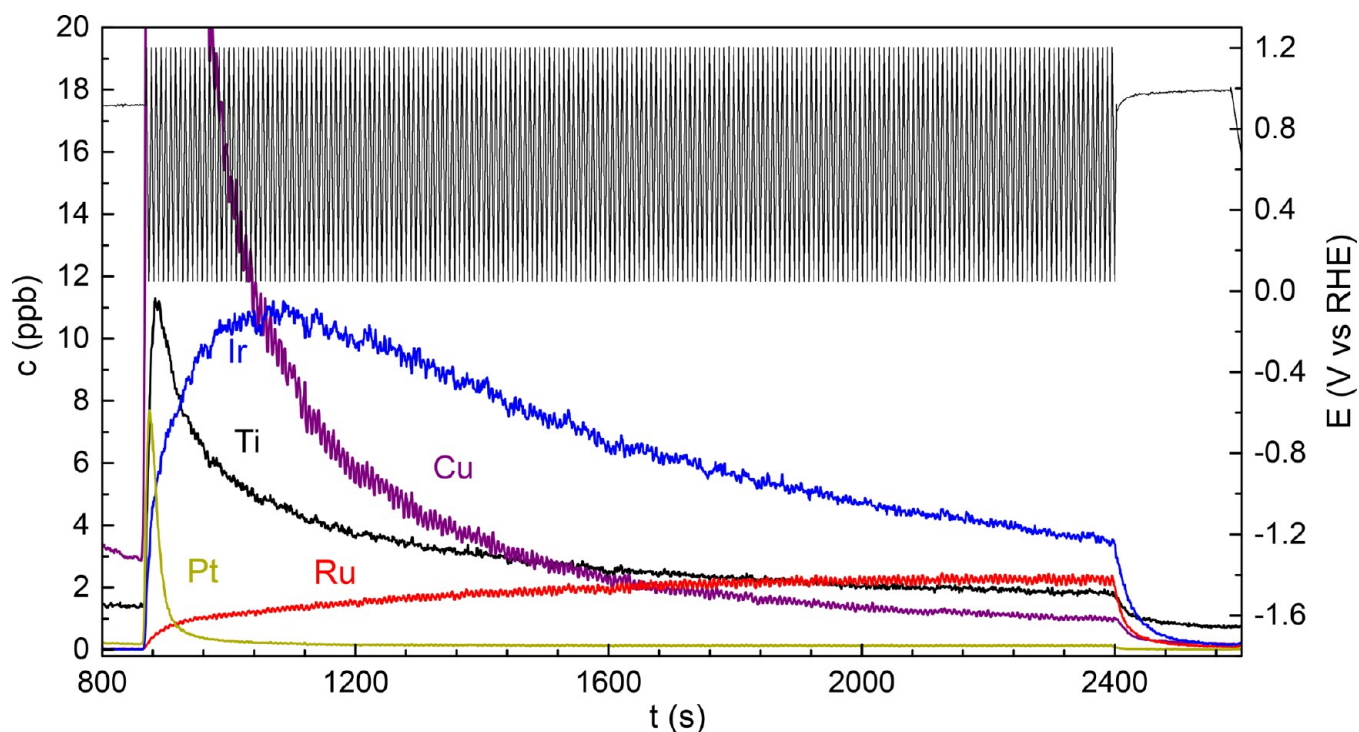


Figure 5. Dissolution profile of the metals during the activation protocol (200 cycles, 300 mV s^{-1} , 0.05 to 1.2 V vs RHE).

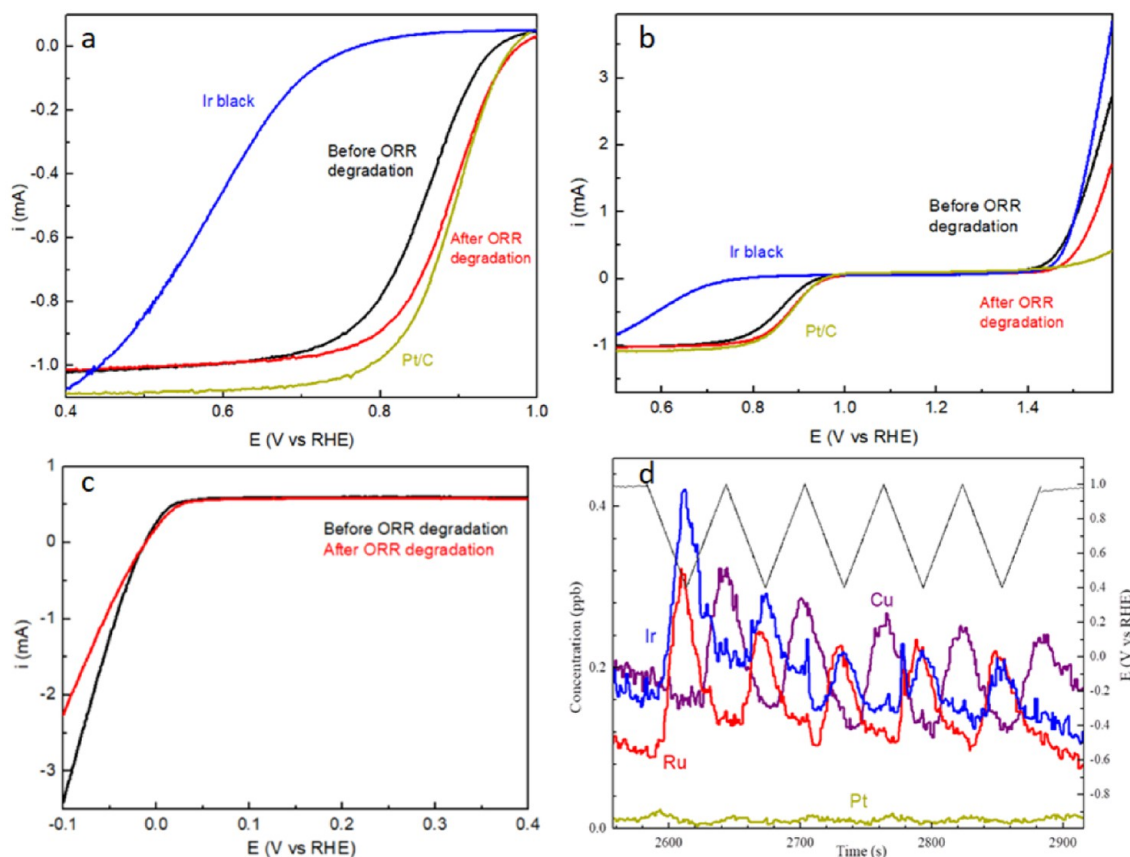


Figure 6. (a) ORR polarization curves before and after degradation – ORR protocol. (b) OER polarization curves before and after degradation – ORR protocol. (c) HOR/HER polarization curves before and after degradation – ORR protocol. (d) The dissolution profile of the precious metal during five cycles from 0.4 to 1.0 V vs RHE. The curves were obtained at 20 mV s^{-1} , in 0.1 M HClO_4 , 1600 rpm, under O_2 (a,b) or H_2 (c) atmosphere.

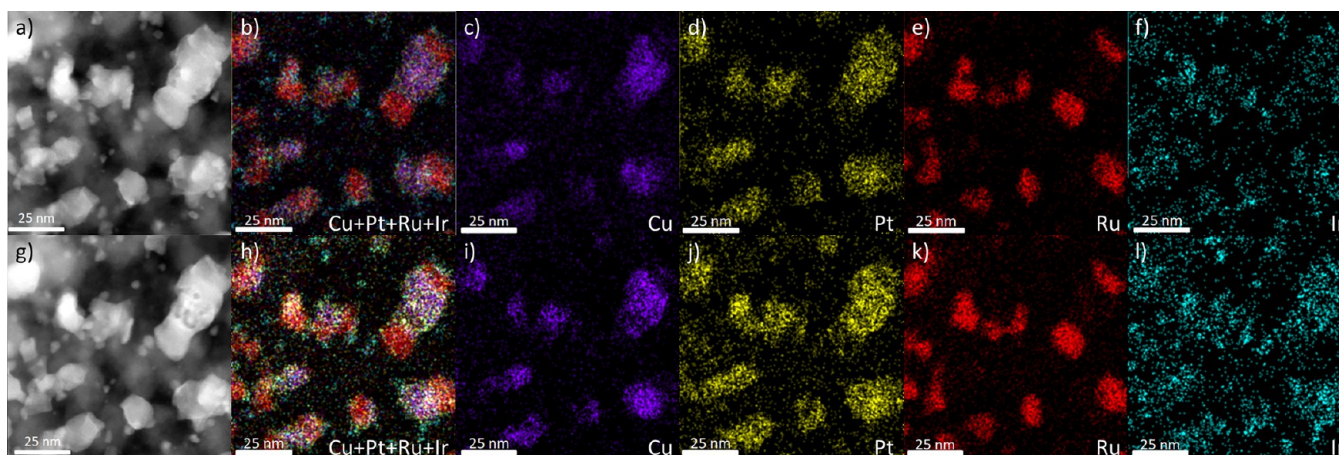


Figure 7. IL-EDX of TiON-RuPtCu-Ir. (a–f) As prepared, (g–l) After ORR degradation. (a,g) STEM ADF images. (b,h) Overlapping of copper (purple), platinum (yellow), ruthenium (red), and iridium (light blue).

analyzed (0.4–1.0 V, 1.2–1.6 V vs RHE, and 0.4–1.6 V vs RHE) with RDE.

Before and in between each of the electrochemical steps, the catalyst was investigated in a separate ex situ experiment for local nanoscale compositional, morphological and structural changes at the same location under SEM and STEM. The so-called identical location (IL) electron microscopy is a unique technique that allows observations of the changes at the same location during different electrochemical biasing like activation, activity measurements, accelerated stress test, and so on.⁷⁴ It provides a clear advantage compared with commonly used microscopy characterization with the assurance that the same location is tracked throughout the history of the studied sample (e.g., same nanoparticle). By contrast, the conventional microscopy of random post-mortem locations provides general statistical insights that are only plausible if numerous locations are evaluated.

c.2. Activation Cycling between 0.05 and 1.2 V vs RHE; Activation Protocol. As noted previously, the electrochemical activation is primordial to reach a good ORR activity in the case of Pt alloy.⁷⁵ The shapes of activation dissolution profiles are different for all five metals in the sample (Figure 5). As expected, Cu aggressively dissolves already at the beginning of the protocol, reaching almost 200 ppb. This phenomenon is usually called dealloying, where Cu is getting selectively leached from the Pt alloy surface and also from the bulk.⁵⁵ The resulting structure is a few layers of Pt on top of copper platinum alloy, which enables the so-called ligand and/or strain effect that is enhancing ORR.^{55,76–78} Dealloying can also result in the formation of a porous structure. However, the Pt-surface still exhibits enhanced ORR activity because of the Cu underneath. All of the noble metals present in the catalyst exhibit dissolution, however with 1 order of magnitude lower rate than Cu. Of course, this slower dissolution is expected as noble metals are known for superior resistance to corrosion. Still, under the present conditions, their dissolution rate is considerably higher than usually observed. This higher rate is mostly due to the so-called transient dissolution mechanism that occurs upon reduction or formation of noble metals oxide.⁷⁹ It is known that noble metals (with the exception of gold) form native oxides when exposed to air and they dissolve during the electrochemical reduction.⁸⁰ For this reason, Pt and Ir exhibit a huge dissolution peak during the first cycles before reaching/trending in the direction of a steady state of low

dissolution. This is in agreement with the dissolution due to the reduction of the native oxides in addition to classical transient dissolution in this potential window. Interestingly, in the case of Ru, the dissolution is slower but starts to increase with the number of cycles. This could be explained by the fact that the potential of 1.2 V vs RHE is enough to produce Ru-oxide, which is increasing with the number of cycles.⁸¹ For that reason, the transient dissolution during oxide reduction increases. During the activation, some Ti is also dissolving. We note that this amount is quite low given that TiON_x is the support (mass ratio of 43.67% of the catalyst) and presents less than 3% (2.4%) of the initial Ti in the catalyst. The dissolution of all the metals for each protocol can be found in the Supporting Information (Table S1). We hypothesize that most of the Ti is stabilized in the support and the unstable superficial Ti is removed during the activation.

c.3. Degradation Cycling between 0.4 and 1.0 V vs RHE; ORR Protocol. The catalyst's activity for ORR, OER, and HER was investigated before and after 10 000 cycles of AST. The stability was evaluated by cycling between 0.4 and 1.0 V vs RHE. The comparison of the polarization curves before and after the AST is presented in Figure 6a–c. The effect of AST is different depending on the reaction. Interestingly, the catalyst is more active for ORR after the degradation test and less active for OER (Figure 6b). The onset for HER does not shift in the degradation test. However, the slope of the reaction decreases after AST (Figure 6c).

The decrease in OER and HER and the increase in ORR activity could be explained by the dissolution of Ir or Ru. In as-synthesized catalysts, both, especially Ru, are covering to significant extent the surface of PtCu nanoparticles (see chemical mapping in Figure 2). This explains the relatively low initial ORR. Later on, however, the superficial amount of Ru and/or Ir decreases and a larger portion of Pt surface becomes available for ORR. At the same time, the decreasing amount of Ir and/or Ru, which are known to be the best OER catalysts,^{48,81,82} results in decreasing activity for OER, as seen in Figure 6b.

The activity of HER also decreases with progressive cycling, particularly at high overpotentials, as shown in Figure 6c. This can be explained by the diminished catalytic contribution of Ru and Ir because of their removal via dissolution. Namely, it has been shown that nanocomposites of Ir on graphene³⁴ and Ru in contact with Pt are good catalysts for HER.⁸³ Finally, the

results of Figure 6 show that the HOR activity at low current density is improved after the degradation protocol. This might be ascribed to the same effect as in the case of the activity trend at high current density, namely the dissolution of Ir and Ru. More specifically, since Pt is a far better HOR catalyst than Ru or Ir, exposing additional Pt surface at the expense of Ru and Ir dissolution is expected to increase HOR activity at low overpotentials.^{84,85}

In continuation, advanced electrochemical characterization techniques IL-STEM and EFC-ICP-MS were used to follow the morphological, structural, and compositional changes of the electrocatalysts. The amount of dissolved metal during five cycles between 0.4 and 1.0 V vs RHE is extremely low for all the metals studied, as can be deduced from Figure 6d. In the on-line dissolution ICP-MS, there is still some washing out of the metals from the activation step before the cycling protocol. This was most pronounced in the case of Ir: the “background” before the first CV cycle (cca 0.17 ppb) was much higher than the “background” just before the activation (cca 0.015 ppb). This peak tailing might be due to the wash-out effect or it might suggest that Ir is more prone to dissolution at OCP after the activation step. Pt and Cu dissolution peaks occur at high potentials (anodic), while the dissolution of Ir and Ru reaches a maximum at low potentials (cathodic). This suggests that Ir and Ru surfaces are covered with corresponding oxides and the dissolution is caused by its reduction at low potentials, in accordance with the literature.^{68,81} Moreover, the amount of Ir dissolved decreases in each cycle, which indicates that less and less of new iridium oxide is formed at this potential protocol. More information about the processes of dissolution can be found in the Supporting Information (Figure S8).

The EFC-ICP-MS results reveal the dissolution dynamics, however, they do not provide local morphological and structural insights. For that reason, IL-EDX and IL-STEM were utilized. Micrographs of the same location of the as-prepared catalyst after activation and after degradation in ORR window are presented in Figure 7 and Figure 8. IL-EDX reveals the nature of each nanostructure. No significant changes in the composition through the degradation (Figure 7 and Figures S12–S14) can be seen. The porosity formation of PtCu nanoparticles can be observed after activation (Figure 8). More figures revealing similar changes can be found in the

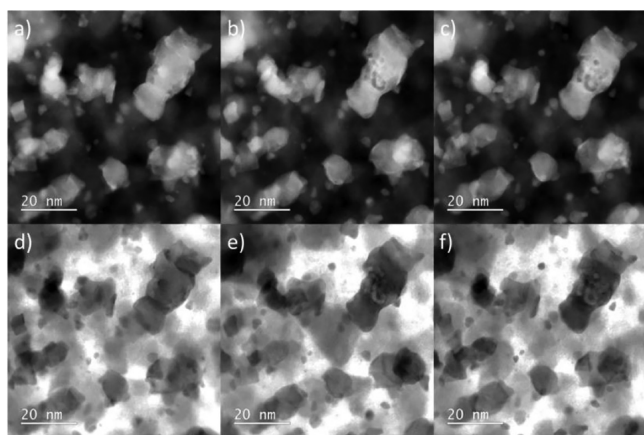


Figure 8. IL-STEM ADF and BF images of TiON-RuPtCu-Ir. (a,d) As-prepared, (b,e) after activation (between 0.05 and 1.2 V vs RHE), and (c,f) after ORR protocol (10 000 cycles between 0.4 and 1.0 V vs RHE).

Supporting Information (Figures S9–11). The results are in accordance with the detected loss of Cu during activation (dealloying) and additionally confirm the known fact that Pt alloys need to be activated in order to display a good ORR activity.⁵⁵ It is unusual that some porosity is already present in the as-synthesized catalyst. We presume that this is due to the complex synthesis where the high standard redox potentials of present noble metals could induce cathodic exchange and oxidize Cu.⁸⁶ Interestingly, after degradation, no significant change can be observed despite the fact that porous PtNi nanoparticles were shown to coarsen at these conditions.⁸⁷ Obviously, in the present case, the formed porosity is stabilized in a certain way. We hypothesize that the presence of Ir or even Ru slows down the surface diffusion of Pt, which is responsible for this particular degradation mechanism.^{62,88}

c.4. Degradation between 1.2 and 1.6 V vs RHE; OER Protocol. The stability during OER operation potentials was tested by cycling 10 000 times between 1.2 and 1.6 V vs RHE. Figure 9a shows the activity for ORR before and after AST. The ORR polarization curve after the degradation is slightly shifted to higher potentials, which increases the activity by around 9%. In the case of OER, Figure 9b, the activity decreases after the stability test by about 61% (i.e., around 39% of the initial activity is remaining, see Table S3 in SI) because of the dissolution of Ru. At the same time, the activity for HER improves, especially at high overpotentials. This is again expected because at this high potential, Ru is intensively dissolving.⁸¹ Less Ru results in a decreased OER and improved ORR activity. Pt and Ir surface become exposed and more active for ORR, respectively, as can be seen in Figure 9c. In order to explain the HER performance trend, more effort is needed. First, it should be noted that in this particular protocol, the HER activity trends for low and high current density region are reversed in comparison to the degradation test carried out between 0.4 and 1.0 V vs RHE (see section 3c above). Namely, in the present case, the HER activity increases at high current density and decreases at low current density region after degradation. In the case of HOR, the activity at low overpotentials is increased after the degradation protocol (Figure 9c). This is in line with Ru and Ir dissolution and exposure of additional Pt surface area. As for the trend in HER, the following is noticed; the activity is increased also after degradation. At a first glance, this is unexpected and difficult to understand. More specifically, after degradation testing between 1.2 and 1.6 V vs RHE agglomeration of nanoparticles is expected. This causes a decrease of the average particle separation distance—hence a change in the local pH, which slows the reaction.

The dissolution dynamics of all five metals was inspected by EFC-ICP-MS (Figure 9d,e). Ru is completely unstable in this potential region⁸¹ and would most likely be completely washed from the sample in a few additional cycles. In five cycles, about 36.5% of total Ru was dissolved. Only anodic peaks are distinguishable, which is in accordance with the Ru OER mechanism that includes the formation of unstable RuO₄.⁸¹ The dissolution of Ru is in good agreement with the loss of activity for OER. There is still noticeable OER activity after degradation since Ir, which is a catalyst used in real PEM electrolyzers, is still present. Nevertheless, Ir is exhibiting some dissolution at high potentials, contrary to the ORR protocol where dissolution is seen only at reductive potentials. Ir is getting oxidized during the anodic potential sweep up to the OER potential range, and thus, in addition to an OER-

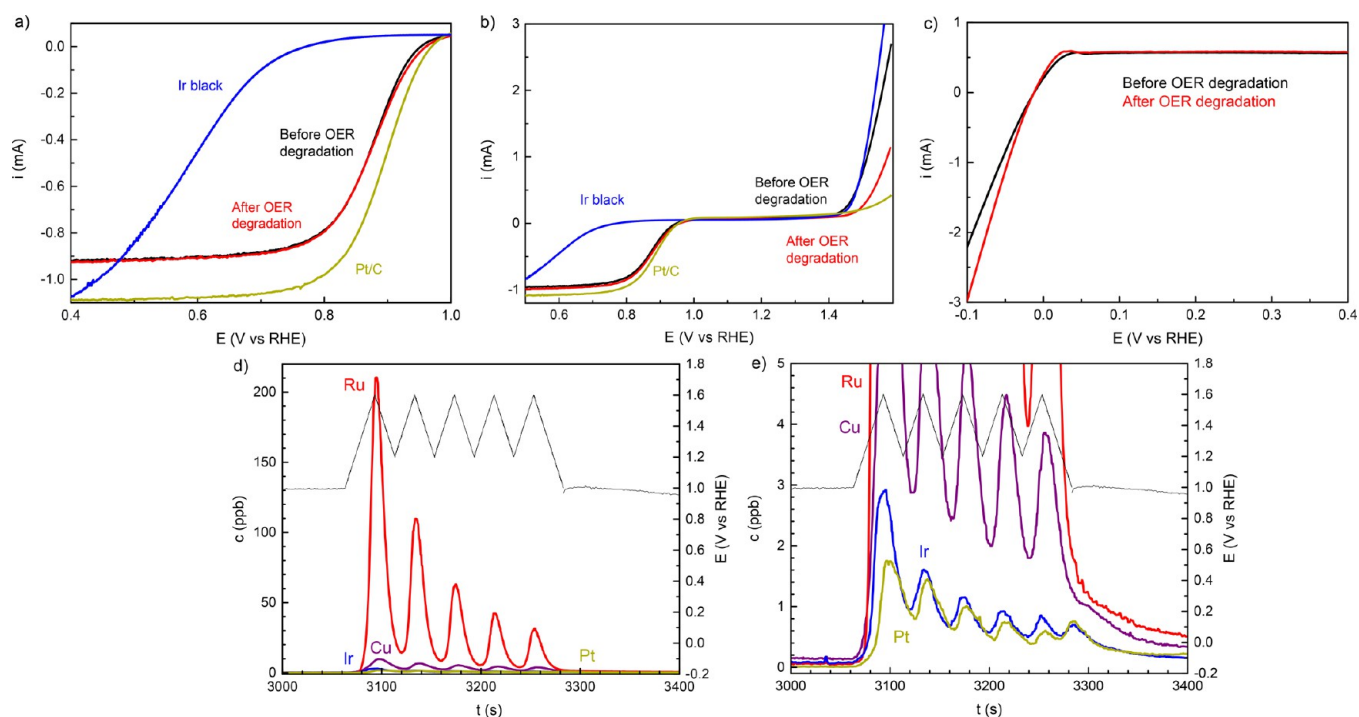


Figure 9. (a) ORR polarization curves before and after degradation – OER protocol. (b) OER polarization curves before and after degradation – OER protocol. (c) HOR/HER polarization curves before and after degradation – OER protocol. (d) The dissolution profile of the precious metal during five cycles from 1.2 to 1.6 V vs RHE. (e) Enlarged view of Pt and Ir dissolution profiles. The curves were obtained at 20 mV s^{-1} , in 0.1 M HClO_4 , 1600 rpm, under O_2 (a and b) or H_2 (c) atmosphere.

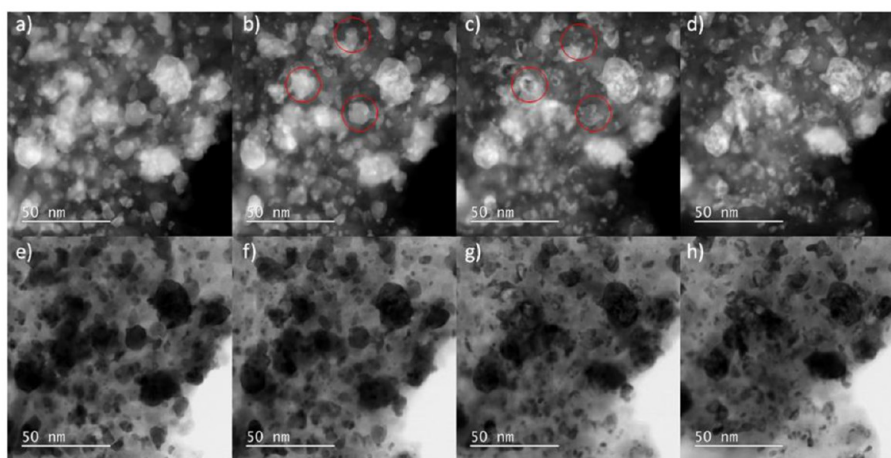


Figure 10. IL-STEM ADF and BF images of TiON-RuPtCu-Ir. (a–e) As-prepared. (b–f) After activation. (c–g) After 10 cycles OER protocol. (d–h) After 10 000 cycles OER protocol.

mediated dissolution, transient dissolution is also taking place.^{80,81,89} The decrease during progressive cycling is probably due to the fact that more and more of Ir is getting irreversibly oxidized. Interestingly, Pt exhibits a similar behavior as Ir. It is getting oxidized, however, and its oxide is not active for OER and is not even sufficiently electrically conductive. Therefore, the dissolution mechanism is not related to OER but in our opinion only to a classical transient dissolution. The dissolution of Cu is mechanically tightly connected with the dissolution of Pt. Whenever Pt is removed from the surface (when it is being dissolved), it uncovers the copper underneath that instantly dissolves as it is unstable at these potentials. Ti, in our opinion, follows the dissolution of

other metals because the latter uncover fresh support surface area (Figure S15).

The IL-STEM and IL-EDX results confirm the massive dissolution of Ru as most of the particles are not present anymore after the degradation (Figures 10 and 11, Figures S16–S21). It can be seen from Figure 10 that Ru already dissolved after only 10 cycles between 1.2 and 1.6 V vs RHE (red circles). The dissolution of Ru also increases the surface area of PtCu as the nanoparticles were in contact before. This can, to a certain degree, explain the increases in HER and ORR activity even with a low Pt dissolution that should decrease the activity. Formation of Pt oxide at high potentials is passivating and thus effectively protecting Pt from corrosion.⁸⁰ However, noticeable morphological changes are

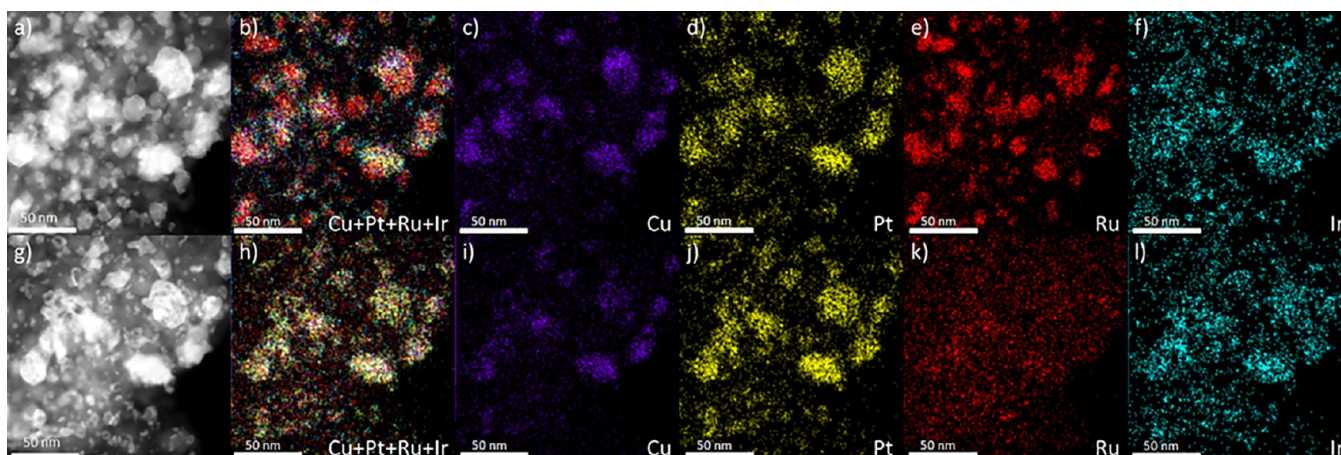


Figure 11. IL-EDX of TiON-RuPtCu-Ir: (a–f) as-prepared, (g–l) after OER degradation, (a,g) STEM ADF images, (b,h) overlapping of copper (purple), platinum (yellow), ruthenium (red), and iridium (light blue).

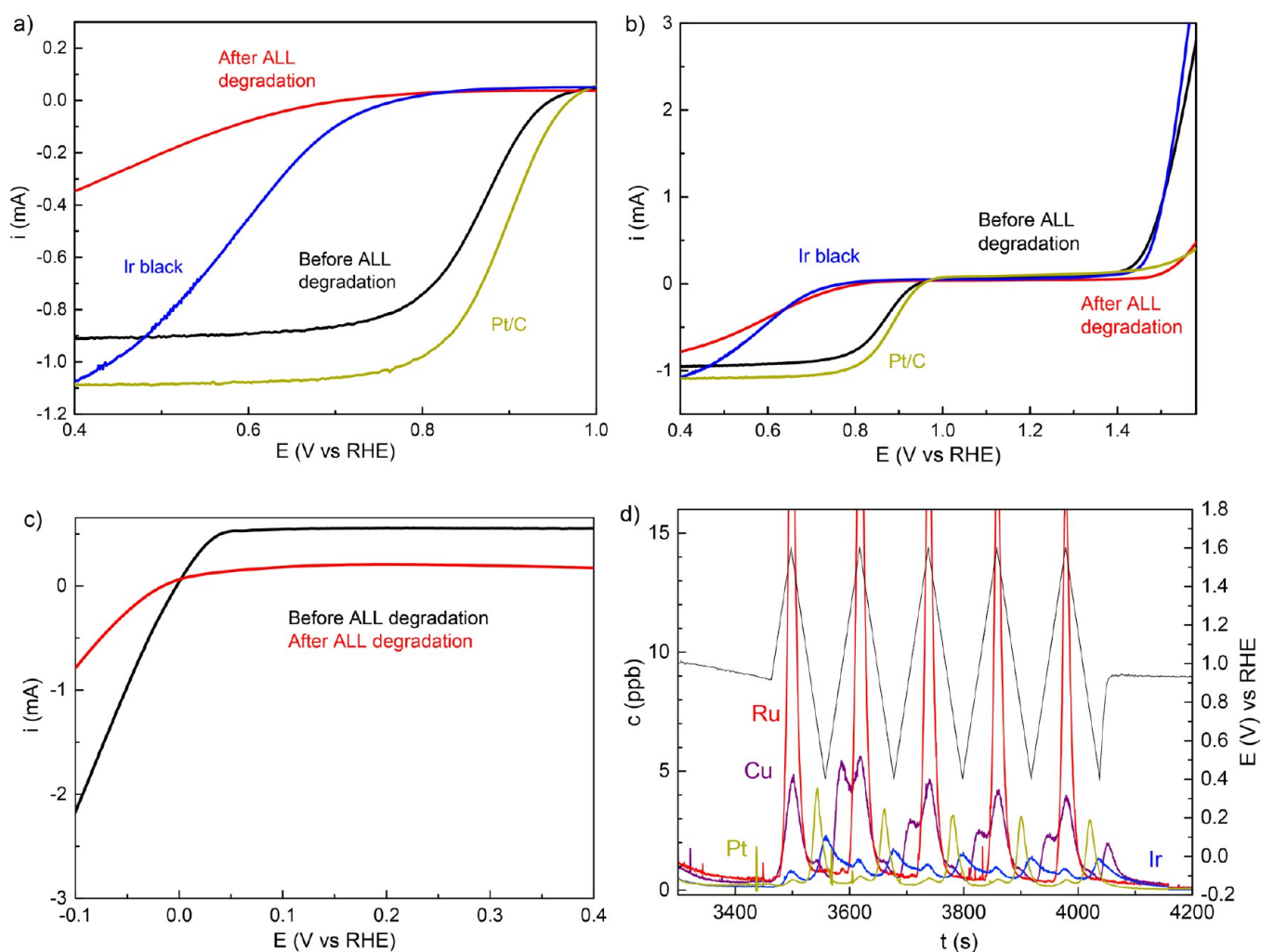


Figure 12. (a) ORR polarization curves before and after degradation – ORR & OER protocol. (b) OER polarization curves before and after degradation – ORR & OER protocol. (c) HOR/HER polarization curves before and after degradation – ORR & OER protocol. (d) Dissolution profile of the precious metal during five cycles from 1.2 to 1.6 V vs RHE. The curves were obtained at 20 mV s^{-1} , in 0.1 M HClO_4 , 1600 rpm, under O_2 (a and b) or H_2 (c) atmosphere.

observed under IL-STEM imaging (Figures 10 and S16–S18). After the OER degradation protocol, Pt nanoparticles change size and shape. This is probably due to the fact that since Ru is getting removed, the remaining Pt particles progressively lose

contact to the support and start migrating toward new stable positions on the support.

c.5. Degradation between 0.4 and 1.6 V vs RHE: ORR & OER Protocol. After cycling between 0.4–1.6 V vs RHE, the

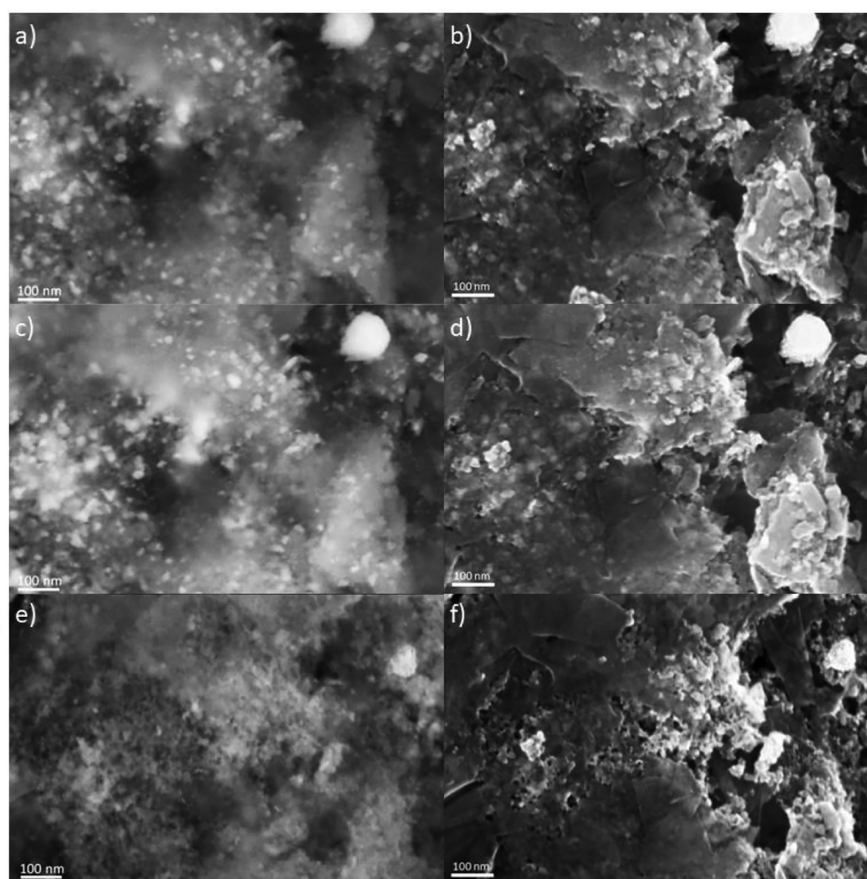


Figure 13. IL-SEM pictures of TiON-RuPtCu-Ir. (a,b) As-prepared. (c,d) After activation. (e,f) After ORR & OER degradation. (a,c,e) Secondary and (b,d,f) in-lens detector.

catalyst's activity severely decreases for all reactions, as seen in Figure 12. The polarization curve for ORR does not present the usual characteristics of a Pt-based catalyst for ORR (e.g., reaching a current of around 1 mA at 0.8 V vs RHE; Figure 12a). Similarly, after the degradation, the activity for HER diminishes almost to zero (Figure 12c). The significant decrease in the activity for these two reactions can be correlated to the almost complete corrosion of PtCu nanoparticles. This is confirmed by the post-mortem STEM EDX chemical mapping micrograph (Figures S23–S26) where a limited number of PtCu particles can be found compared to the “as prepared” or “activated” samples. It is known that Pt exhibits severe transient dissolution when repetitively oxidized and completely reduced, that is cycled between 0.4 and 1.6 V vs RHE.^{73,90,91} However, the decrease of activity could also be due to the degradation of the support as can be observed in the IL-SEM in Figure 13 (and Figure S27). The IL-SEM pictures were taken with two different detectors, which allowed us to observe more effectively the phenomena happening on the surface (InLens detector, Figure 13b,d,f), and inside the catalyst surface structure (secondary electron detector, Figure 13a,c,e).

Pt has a typical dissolution profile with low anodic and high cathodic peaks. The cathodic peaks increase when the potential is still decreasing. This is to be expected for a complete reduction of the surface oxide. As Pt dissolves, the remaining Cu dissolves accordingly. The EFC-ICP-MS dissolution profile (Figure 12d) proves the link between the two phenomena by the apparition of an anodic peak for Cu during the second

cycle, which it is not present in the first peak (scanning from OCP to 1.6 V vs RHE) and is caused by the venture to potentials lower than OCP (cca. 1 V). This peak is attributed to the dissolution of the deposited Cu. Moreover, the highest dissolution peaks for Cu are anodic peaks. After each anodic peak, there is a small cathodic shoulder that gets more and more blended into the anodic peak with each cycle. This is in accordance with our recent study on a pure PtCu-based catalyst.⁹²

In the case of OER, the activity decreases by a factor of 6, as can be extracted from Figure 12b. The complete dissolution of Ru (no particles found in STEM imaging after degradation) contributes to this decrease. It explains the activity decay after this severe ADT.

The Ru dissolution is approximately 10 times faster than Ir dissolution. It exhibits predominantly anodic dissolution, as in the OER protocol—the main peaks are completely separated. In the Ir dissolution profile, anodic and cathodic peaks are well-defined. The cathodic dissolution is larger than the anodic. As opposed to Ru, the concentration during cycling does not fall to the background level—even the regions between the peaks show significant dissolution. In the last cycle that ends at OCP instead of 1.6 V, there is no anodic dissolution. Cathodic dissolution is the most pronounced at the lowest potential and there is no peak separation. This suggests that the reduction of oxide species is not complete (as it is in the case of Pt)—there is still iridium oxide present. At prolonged exposure to low potentials, this cathodic dissolution

might continue; however, it is known that at these conditions, Ir electro-oxidation is not reversible.⁷⁹

Ti dissolution is increased (compared with the background level) during all five cycles. There are distinct anodic peaks and smaller cathodic peaks in between (perhaps not totally symmetrically placed between two anodic peaks). This could explain the degradation of the support. We presume that the dissolved Ti could be due to corrosion of other metals that exposes new, fresh surface of Ti support. If Ti does not protect the graphene anymore, the latter can be destroyed.

As noted before, the wide potential window causes that all noble metals are exhibiting transient oxidation and reduction during cycling. As shown by Cherevko et al., this process induces transient dissolution of noble metals.⁷⁹ The dissolution profiles in Figure 12d are in accordance with that study. For each metal, two or three peaks can be observed. Because of the high scan rate (20 mV s^{-1}), the resolution of the peak is not appropriate to clearly define an onset potential, but anodic and cathodic processes can still be distinguished for each metal.

EDX during IL-SEM was used to determine the atomic ratio of the precious metal after different steps (as-prepared, after activation, and after degradation) as seen in Table S2. This confirms the faster dissolution of Ru and Cu compared with Pt and Ir.

c.6. Resume: "Practical Guidelines for the Appropriate Use or What Not to Do". TiON-RuPtCu-Ir is a multifunctional catalyst that can be used for many reactions such as ORR, OER, HER, or MOR. However, the stability of the different metals depends on the potential window used. Thus, the utility of this material depends on how we plan to use it. First of all, one must choose the appropriate activation protocol not to damage the needed active sites. Indeed, the catalyst is stable during ORR (and HER as seen in Figure 14,

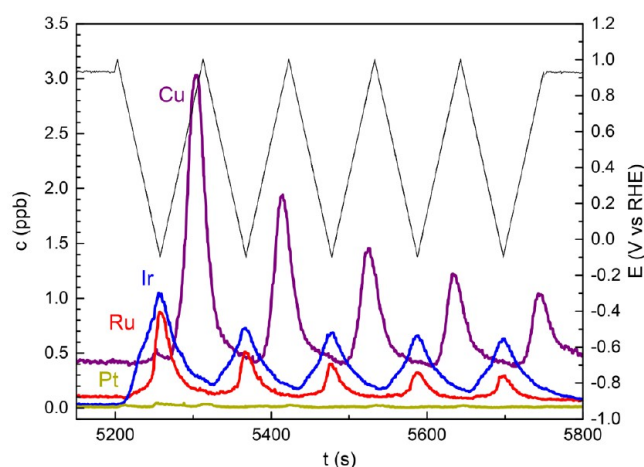


Figure 14. Dissolution profile of the various metals found in present sample during 5 cycles from -0.1 to 1.0 V vs RHE .

where the dissolution of all metals is low) and semistable at OER. OER was shown to dissolve Ru but interestingly does not affect Pt (as a protective oxide layer is formed). However, when the cycling is extended over the potential window of both reactions (from 0.4 to 1.6 V vs RHE), the degradation is severe for all metals. Also, if Ru is needed for the MOR, high potentials should be avoided. A typical upper limit of 1 V vs RHE should be considered. In contrast, if Ir needs to stay intact, transitions between ORR potential window (0.4 to 1.0

V vs RHE) and OER potential window (1.2 to 1.6 V vs RHE) should be avoided. Ir mostly dissolved during the ORR & OER protocol. In the same way, this window is destructive for Pt. Also, because of exposure of fresh sites of the support, the usage of the same window also promotes the dissolution of "unstable" Ti that did not dissolve during activation. Interestingly, Ir and Ru also dissolve if preoxidized at HER conditions (Figure 14). An overview of how the activity changes for ORR, OER, and HER after the degradation in different potential windows can be found in Table S3.

4. CONCLUSIONS

A highly active multifunctional catalyst consisting of PtCu alloy, Ru, and Ir on graphene-based TiON_x support was successfully synthesized. The micrometer-sized graphene flakes were evenly covered with a TiON_x layer onto which the respective noble metal nanoparticles were attached. The multifunctional catalyst exhibited a 3 times higher mass activity than the Pt/C benchmark for ORR and 10 times higher mass activity than Ir black benchmark for OER. It also has an overpotential window, ΔE , of 0.651 V , which is lower than that of the physically mixed state-of-the-art Pt–Ir bifunctional catalyst. Moreover, the catalyst also exhibits a high activity for hydrogen evolution and oxidation reactions as well as for MOR.

The stability of the catalyst with the different potential windows was investigated with online-ICP-MS and IL-TEM. Three different aging protocols were used to represent the conditions of oxygen-involved reactions. After the ORR protocol, the catalyst still showed high activities for all the reactions. Even after a 45% loss of activity for OER, the mass activity is around 5 times better than that of the fresh Ir black benchmark. After the OER protocol, Ru was almost completely dissolved. Interestingly, the activities for ORR and HER even increased. The third protocol (i.e., cycling between 0.4 and 1.6 V vs RHE) had the most damaging effect on the catalyst. Indeed, almost all the activity was lost after 10 000 cycles for all the reactions. From a practical point, our study enlightens the importance of the degradation effect of cycling between ORR and OER regions. It may be expected that the results will contribute to a better understanding of which cycling treatment should be chosen in order to prevent the needed active metals from dissolving and thus achieving the appropriate catalyst activation.

■ ASSOCIATED CONTENT

Supporting Information

The Supporting Information is available free of charge on the ACS Publications website at DOI: [10.1021/acscatal.9b03385](https://doi.org/10.1021/acscatal.9b03385).

Synthesis, XRD, EDX, mass-normalized comparison with benchmarks, ICP-MS protocol, ICP-MS-ORR degradation, IL-TEM/IL-EDX – ORR degradation, ICP-MS-OER degradation, IL-TEM/IL-EDX – OER degradation, ICP-MS-ORR & OER degradation, IL-SEM/IL-EDX – ORR & OER degradation, amount of dissolved metal during (ICP-MS), atomic ratios, table of activity changes after degradation, ICP-MS – 5 cycles from 0 to 1.6 V (PDF)

■ AUTHOR INFORMATION

Corresponding Authors

*E-mail: marjan.bele@ki.si

*E-mail: nejc.hodnik@ki.si.

ORCID

Alen Vizintin: 0000-0003-1876-1396

Primož Jovanovič: 0000-0003-2477-3895

Martin Sala: 0000-0001-7845-860X

Miran Gaberšček: 0000-0002-8104-1693

Nejc Hodnik: 0000-0002-7113-9769

Notes

The authors declare no competing financial interest.

ACKNOWLEDGMENTS

This study was supported by the Slovenian Research Agency for the research programme P2-0152, P1-0034, and P2-0393 and projects Z2-8161, N2-0106, and Z1-9165.

REFERENCES

- (1) Schlogl, R. The Role of Chemistry in the Energy Challenge. *ChemSusChem* **2010**, *3*, 209–222.
- (2) Barreto, L.; Makihiro, A.; Riahi, K. The Hydrogen Economy in the 21st Century. *Int. J. Hydrogen Energy* **2003**, *28*, 267–284.
- (3) Perry, M. L.; Fuller, T. F. A Historical Perspective of Fuel Cell Technology in the 20th Century. *J. Electrochem. Soc.* **2002**, *149*, S59–S67.
- (4) Lee, S. W.; Carlton, C.; Risch, M.; Surendranath, Y.; Chen, S.; Furutsuki, S.; Yamada, A.; Nocera, D. G.; Shao-Horn, Y. The Nature of Lithium Battery Materials under Oxygen Evolution Reaction. *J. Am. Chem. Soc.* **2012**, *134*, 16959–16962.
- (5) Carmo, M.; Fritz, D. L.; Mergel, J.; Stolten, D. A Comprehensive Review on PEM Water Electrolysis. *Int. J. Hydrogen Energy* **2013**, *38*, 4901–4934.
- (6) Notton, G.; Nivet, M.-L.; Voyant, C.; Paoli, C.; Darras, C.; Motte, F.; Fouilloy, A. Intermittent and Stochastic Character of Renewable Energy Sources: Consequences, Cost of Intermittence and Benefit of Forecasting. *Renewable Sustainable Energy Rev.* **2018**, *87*, 96–105.
- (7) Katsounaros, I.; Cherevko, S.; Zeradhanin, A. R.; Mayrhofer, K. J. Oxygen Electrochemistry as a Cornerstone for Sustainable Energy Conversion. *Angew. Chem., Int. Ed.* **2014**, *53*, 102–121.
- (8) Katsounaros, I.; Koper, M. T. M. Electrocatalysis for the Hydrogen Economy. In *Electrochemical Science for a Sustainable Society*; Uosaki, K., Ed.; Springer: Cham, 2017; pp 23–50.
- (9) Paul, B.; Andrews, J. PEM Uninitiated Reversible/Regenerative Hydrogen Fuel Cell Systems: State of the Art and Technical Challenges. *Renewable Sustainable Energy Rev.* **2017**, *79*, S85–S99.
- (10) Park, S.; Shao, Y.; Liu, J.; Wang, Y. Oxygen Electrocatalysts for Water Electrolyzers and Reversible Fuel Cells: Status and Perspective. *Energy Environ. Sci.* **2012**, *5*, 9331–9344.
- (11) Wang, Y.; Leung, D. Y. C.; Xuan, J.; Wang, H. A Review on Uninitiated Regenerative Fuel Cell Technologies, Part-A: Uninitiated Regenerative Proton Exchange Membrane Fuel Cells. *Renewable Sustainable Energy Rev.* **2016**, *65*, 961–977.
- (12) Antolini, E. Iridium As Catalyst and Cocatalyst for Oxygen Evolution/Reduction in Acidic Polymer Electrolyte Membrane Electrolyzers and Fuel Cells. *ACS Catal.* **2014**, *4*, 1426–1440.
- (13) Zhigang, S.; Baolian, Y.; Ming, H. Bifunctional Electrodes with a Thin Catalyst Layer for Uninitiated Proton Exchange Membrane Regenerative Fuel Cell. *J. Power Sources* **1999**, *79*, 82–85.
- (14) Ioroi, T.; Kitazawa, N.; Yasuda, K.; Yamamoto, Y.; Takenaka, H. Iridium Oxide/Platinum Electrocatalysts for Uninitiated Regenerative Polymer Electrolyte Fuel Cells. *J. Electrochem. Soc.* **2000**, *147*, 2018–2022.
- (15) Jung, H.-Y.; Park, S.; Popov, B. N. Electrochemical Studies of an Unsupported PtIr Electrocatalyst as a Bifunctional Oxygen Electrode in a Uninitiated Regenerative Fuel Cell. *J. Power Sources* **2009**, *191*, 357–361.
- (16) da Silva, G. C.; Mayrhofer, K. J. J.; Ticianelli, E. A.; Cherevko, S. Dissolution Stability: The Major Challenge in the Regenerative Fuel Cells Bifunctional Catalysis. *J. Electrochem. Soc.* **2018**, *165*, F1376–F1384.
- (17) da Silva, G. C.; Fernandes, M. R.; Ticianelli, E. A. Activity and Stability of Pt/IrO₂ Bifunctional Materials as Catalysts for the Oxygen Evolution/Reduction Reactions. *ACS Catal.* **2018**, *8*, 2081–2092.
- (18) Yao, W.; Yang, J.; Wang, J.; Nuli, Y. Chemical Deposition of Platinum Nanoparticles on Iridium Oxide for Oxygen Electrode of Uninitiated Regenerative Fuel Cell. *Electrochem. Commun.* **2007**, *9*, 1029–1034.
- (19) Zhang, Y.; Zhang, H.; Ma, Y.; Cheng, J.; Zhong, H.; Song, S.; Ma, H. A Novel Bifunctional Electrocatalyst for Uninitiated Regenerative Fuel Cell. *J. Power Sources* **2010**, *195*, 142–145.
- (20) Kong, F. D.; Liu, J.; Ling, A. X.; Xu, Z. Q.; Shi, M. J.; Kong, Q. S.; Wang, H. Y. Overlapping Structure of Platinum-Iridium Oxide Layers and its Electrocatalytic Behavior on Bifunctional Oxygen Electrode. *Catal. Commun.* **2017**, *90*, 19–22.
- (21) Kong, F.-D.; Zhang, S.; Yin, G.-P.; Liu, J.; Ling, A.-X. A Facile Route to Fabricate Effective Pt/IrO₂ Bifunctional Catalyst for Uninitiated Regenerative Fuel Cell. *Catal. Lett.* **2014**, *144*, 242–247.
- (22) da Silva, G. C.; Mayrhofer, K. J. J.; Ticianelli, E. A.; Cherevko, S. The Degradation of Pt/IrO_x Oxygen Bifunctional Catalysts. *Electrochim. Acta* **2019**, *308*, 400–409.
- (23) Ioroi, T.; Kitazawa, N.; Yasuda, K.; Yamamoto, Y.; Takenaka, H. IrO₂-deposited Pt Electrocatalysts for Uninitiated Regenerative Polymer Electrolyte Fuel Cells. *J. Appl. Electrochem.* **2001**, *31*, 1179–1183.
- (24) Baglio, V.; D'Urso, C.; Di Blasi, A.; Ornelas, R.; Arriaga, L. G.; Antonucci, V.; Arico, A. S. Investigation of IrO₂/Pt Electrocatalysts in Uninitiated Regenerative Fuel Cells. *Int. J. Electrochem.* **2011**, *2011*, Article ID 276205.
- (25) Ye, F.; Xu, C.; Liu, G.; Li, J.; Wang, X.; Du, X.; Lee, J. K. A Novel PtRuIr Nanoclusters Synthesized by Selectively Electrodepositing Ir on PtRu as Highly Active Bifunctional Electrocatalysts for Oxygen Evolution and Reduction. *Energy Convers. Manage.* **2018**, *155*, 182–187.
- (26) Gutsche, C.; Moeller, C. J.; Knipper, M.; Borchert, H.; Parisi, J.; Plaggenborg, T. Synthesis, Structure, and Electrochemical Stability of Ir-decorated RuO₂ Nanoparticles and Pt Nanorods as Oxygen Catalysts. *J. Phys. Chem. C* **2016**, *120*, 1137–1146.
- (27) Parry, S. J. Abundance and Distribution of Palladium, Platinum, Iridium and Gold in some Oxide Minerals. *Chem. Geol.* **1984**, *43*, 115–125.
- (28) Ledendecker, M.; Geiger, S.; Hengge, K.; Lim, J.; Cherevko, S.; Mingers, A. M.; Göhl, D.; Fortunato, G. V.; Jalalpoor, D.; Schüth, F.; Scheu, C.; Mayrhofer, K. J. J. Towards Maximized Utilization of Iridium for the Acidic Oxygen Evolution Reaction. *Nano Res.* **2019**, *12*, 2275–2280.
- (29) Puthiyapura, V. K.; Pasupathi, S.; Su, H. N.; Liu, X. T.; Pollet, B.; Scott, K. Investigation of Supported IrO₂ as Electrocatalyst for the Oxygen Evolution Reaction in Proton Exchange Membrane Water Electrolyser. *Int. J. Hydrogen Energy* **2014**, *39*, 1905–1913.
- (30) Campbell, C. T. Catalyst-Support Interactions: Electronic Perturbations. *Nat. Chem.* **2012**, *4*, 597–598.
- (31) Huang, S.-H.; Ganesan, P.; Park, S.; Popov, B. N. Development of a Titanium Dioxide-supported Platinum Catalyst with Ultrahigh Stability for Polymer Electrolyte Membrane Fuel Cell Applications. *J. Am. Chem. Soc.* **2009**, *131*, 13898–13899.
- (32) Lee, B.-S.; Park, H.-Y.; Cho, M. K.; Jung, J. W.; Kima, H.-J.; Henkensmeier, D.; Yoo, S. J.; Kim, J. Y.; Park, S.; Lee, K.-Y.; Jang, J. H. Development of Porous Pt/IrO₂/Carbon Paper Electrocatalysts with Enhanced Mass Transport as Oxygen Electrodes in Uninitiated Regenerative Fuel Cells. *Electrochem. Commun.* **2016**, *64*, 14–17.
- (33) Kim, I. G.; Nah, I. W.; Oh, I.-H.; Park, S. Crumpled rGO-supported Pt-Ir Bifunctional Catalyst Prepared by Spray Pyrolysis for Uninitiated Regenerative Fuel Cells. *J. Power Sources* **2017**, *364*, 215–225.

- (34) Zhang, J.; Wang, G.; Liao, Z.; Zhang, P.; Wang, F.; Zhuang, X.; Zschech, E.; Feng, X. Iridium Nanoparticles Anchored on 3D Graphite Foam as a Bifunctional Electrocatalyst for Excellent Overall Water Splitting in Acidic Solution. *Nano Energy* **2017**, *40*, 27–33.
- (35) Pizzutilo, E.; Geiger, S.; Grote, J.-P.; Mingers, A.; Mayrhofer, K. J. J.; Arenz, M.; Cherevko, S. On the Need of Improved Accelerated Degradation Protocols (ADPs): Examination of Platinum Dissolution and Carbon Corrosion in Half-cell Tests. *J. Electrochem. Soc.* **2016**, *163*, F1510–F1514.
- (36) Maass, S.; Finsterwalder, F.; Frank, G.; Hartmann, R.; Merten, C. Carbon Support Oxidation in PEM Fuel Cell Cathodes. *J. Power Sources* **2008**, *176*, 444–451.
- (37) Jang, S.-E.; Kim, H. Effect of Water Electrolysis Catalysts on Carbon Corrosion in Polymer Electrolyte Membrane Fuel Cells. *J. Am. Chem. Soc.* **2010**, *132*, 14700–14701.
- (38) Fuentes, R. E.; Colon-Mercado, H. R.; Martinez-Rodriguez, M. J. Pt-Ir/TiC Electrocatalysts for PEM Fuel Cell/Electrolyzer Process. *J. Electrochem. Soc.* **2014**, *161*, F77–F82.
- (39) Chen, G.; Bare, S. R.; Mallouk, T. E. Development of Supported Bifunctional Electrocatalysts for Unitized Regenerative Fuel Cells. *J. Electrochem. Soc.* **2002**, *149*, A1092–A1099.
- (40) Won, J.-E.; Kwak, D.-H.; Han, S.-B.; Park, H.-S.; Park, J.-Y.; Ma, K.-B.; Kim, D.-H.; Park, K.-W. PtIr/Ti4O7 as a Bifunctional Electrocatalyst for Improved Oxygen Reduction and Oxygen Evolution Reactions. *J. Catal.* **2018**, *358*, 287–294.
- (41) Oakton, E.; Lebedev, D.; Povia, M.; Abbott, D. F.; Fabbri, E.; Fedorov, A.; Nachtegaal, M.; Copéret, C.; Schmidt, T. J. IrO₂-TiO₂: A High-Surface-Area, Active, and Stable Electrocatalyst for the Oxygen Evolution Reaction. *ACS Catal.* **2017**, *7*, 2346–2352.
- (42) Huang, S.-Y.; Ganesan, P.; Jung, H.-Y.; Popov, B. N. Development of Supported Bifunctional Oxygen Electrocatalysts and Corrosion-Resistant Gas Diffusion Layer for Unitized Regenerative Fuel Cell Applications. *J. Power Sources* **2012**, *198*, 23–29.
- (43) Huang, S.-Y.; Ganesan, P.; Popov, B. N. Titania Supported Platinum Catalyst with High Electrocatalytic Activity and Stability for Polymer Electrolyte Membrane Fuel Cell. *Appl. Catal., B* **2011**, *102*, 71–77.
- (44) Moreno, J. J. G.; Fronzi, M.; Lovera, P.; O’Riordan, A.; Nolan, M. Stability of Adsorbed Water on TiO-TiN Interfaces. A First Principles and Ab Initio Thermodynamics Investigation. *J. Phys. Chem. C* **2018**, *122*, 15395–15408.
- (45) Li, G.; Li, K.; Yang, L.; Chang, J.; Ma, R.; Wu, Z.; Ge, J.; Liu, C.; Xing, W. Boosted Performance of Ir Species by Employing TiN as the Support toward Oxygen Evolution Reaction. *ACS Appl. Mater. Interfaces* **2018**, *10*, 38117–38124.
- (46) Zhang, C.; Shen, X.; Pan, Y.; Peng, Z. A Review of Pt-based Electrocatalysts for Oxygen Reduction Reaction. *Frontiers in Energy* **2017**, *11*, 268–285.
- (47) Suen, N.-T.; Hung, S.-F.; Quan, Q.; Zhang, N.; Xu, Y.-J.; Chen, H. M. Electrocatalysis for the Oxygen Evolution Reaction: Recent Development and Future Perspectives. *Chem. Soc. Rev.* **2017**, *46*, 337–365.
- (48) Siracusano, S.; Hodnik, N.; Jovanovic, P.; Ruiz-Zepeda, F.; Šala, M.; Baglio, V.; Aricò, A. S. New insights into the Stability of a High Performance Nanostructured Catalyst for Sustainable Water Electrolysis. *Nano Energy* **2017**, *40*, 618–632.
- (49) Trasatti, S. Surface Science and Electrochemistry: Concepts and Problems. *Surf. Sci.* **1995**, *335*, 1–9.
- (50) Watanabe, M.; Uchida, M.; Motoo, S. Preparation of Highly Dispersed Pt + Ru Alloy Clusters and the Activity for the Electrooxidation of Methanol. *J. Electroanal. Chem. Interfacial Electrochem.* **1987**, *229*, 395–406.
- (51) Marcano, D. C.; Kosynkin, D. V.; Berlin, J. M.; Smit’skii, A.; Sun, Z.; Slesarev, A.; Alemany, L. B.; Lu, W.; Tour, J. M. Improved Synthesis of Graphene Oxide. *ACS Nano* **2010**, *4*, 4806–4814.
- (52) van der Vliet, D.; Strmcnik, D. S.; Wang, C.; Stamenkovic, V. R.; Markovic, N. M.; Koper, M. T. M. On the Importance of Correcting for the Uncompensated Ohmic Resistance in Model Experiments of the Oxygen Reduction Reaction. *J. Electroanal. Chem.* **2010**, *647*, 29–34.
- (53) Hodnik, N.; Jeyabharathi, C.; Meier, J. C.; Kostka, A.; Phani, K. L.; Rečnik, A.; Bele, M.; Hočevar, S.; Gabersček, M.; Mayrhofer, K. J. J. Effect of Ordering of PtCu₃ Nanoparticle Structure on the Activity and Stability for the Oxygen Reduction Reaction. *Phys. Chem. Chem. Phys.* **2014**, *16*, 13610–13615.
- (54) Hodnik, N.; Zorko, M.; Bele, M.; Hočevar, S.; Gabersček, M. Identical Location Scanning Electron Microscopy: A Case Study of Electrochemical Degradation of PtNi Nanoparticles Using a New Nondestructive Method. *J. Phys. Chem. C* **2012**, *116*, 21326–21333.
- (55) Gatalo, M.; Jovanović, P.; Ruiz-Zepeda, F.; Pavlišić, A.; Robba, A.; Bale, M.; Dražić, G.; Gabersček, M.; Hodnik, N. Insights into Electrochemical Dealloying of Cu out of Au-doped Pt-alloy Nanoparticles at the Sub-Nano-Scale. *J. Electrochem. Sci. Eng.* **2018**, *8*, 87–100.
- (56) Zhang, Y.; Franklin, N. W.; Chen, R. J.; Dai, H. Metal Coating on Suspended Carbon Nanotubes and its Implication to Metal-tube Interaction. *Chem. Phys. Lett.* **2000**, *331*, 35–41.
- (57) Zhang, Y.; Dai, H. Formation of Metal Nanowires on Suspended Single-Walled Carbon Nanotubes. *Appl. Phys. Lett.* **2000**, *77*, 3015–3017.
- (58) *Binary Alloy Phase Diagrams*, 2nd ed.; Massalski, T. B., Okamoto, H., Subramanian, P. R., Kacprzak, L., Eds.; ASM International: Materials Park, OH, 1990.
- (59) Trasatti, S. Electrocatalysis: Understanding the Success of DSA. *Electrochim. Acta* **2000**, *45*, 2377–2385.
- (60) Bele, M.; Jovanović, P.; Pavlišić, A.; Jozinović, B.; Zorko, M.; Rečnik, A.; Chernyshova, E.; Hočevar, S.; Hodnik, N.; Gabersček, M. A Highly Active PtCu₃ Intermetallic Core-shell, Multilayered Pt-skin, Carbon Embedded Electrocatalyst Produced by a Scale-up Sol-gel Synthesis. *Chem. Commun.* **2014**, *50*, 13124–13126.
- (61) Hutchinson, J. M. Solubility Relationships in the Ruthenium-Platinum System. *Platinum Met. Rev.* **1972**, *16*, 88–90.
- (62) Jovanovic, P.; Bele, M.; Šala, M.; Ruiz-Zepeda, F.; Dražić, G.; Zabukovec Logar, N.; Nejc Hodnik, N.; Gabersček, M. Corrosion Protection of Platinum-based Electrocatalyst by Ruthenium Surface Decoration. *ACS Appl. Energy Mater.* **2018**, *1*, 3190–3197.
- (63) Alia, S. M.; Hurst, K. E.; Kocha, S. S.; Pivovar, B. S. Mercury Underpotential Deposition to Determine Iridium and Iridium Oxide Electrochemical Surface Areas. *J. Electrochem. Soc.* **2016**, *163*, F3051–F3056.
- (64) Mayrhofer, K. J. J.; Arenz, M.; Blizanac, B. B.; Stamenkovic, V.; Ross, P. N.; Markovic, N. M. CO Surface Electrochemistry on Pt-nanoparticles: A Selective Review. *Electrochim. Acta* **2005**, *50*, S144–S154.
- (65) Gorlin, Y.; Jaramillo, T. F. A Bifunctional Nonprecious Metal Catalyst for Oxygen Reduction and Water Oxidation. *J. Am. Chem. Soc.* **2010**, *132*, 13612–13614.
- (66) Masa, J.; Xia, W.; Sinev, I.; Zhao, A.; Sun, Z.; Grutzke, S.; Weide, P.; Muhler, M.; Schuhmann, W. Mn(x)O(y)/NC and Co(x)O(y)/NC Nanoparticles Embedded in a Nitrogen-doped Carbon Matrix for High-performance Bifunctional Oxygen Electrodes. *Angew. Chem., Int. Ed.* **2014**, *53*, 8508–8512.
- (67) Jiao, Y.; Zheng, Y.; Jaroniec, M.; Zhang Qiao, S. Design of Electrocatalysts for Oxygen- and Hydrogen-involving Energy Conversion Reactions. *Chem. Soc. Rev.* **2015**, *44*, 2060–2086.
- (68) Cherevko, S.; Geiger, S.; Kasian, O.; Kulyk, N.; Grote, J.-P.; Savan, A.; Shrestha, B. R.; Merzlikin, S.; Breitbach, B.; Ludwig, A.; Mayrhofer, K. J. J. Oxygen and Hydrogen Evolution Reactions on Ru, RuO₂, Ir, and IrO₂ Thin Film Electrodes in Acidic and Alkaline Electrolytes: A Comparative Study on Activity and Stability. *Catal. Today* **2016**, *262*, 170–180.
- (69) Yao, Y.; Hu, S.; Chen, W.; Huang, Z.-Q.; Wei, W.; Yao, T.; Liu, R.; Zang, K.; Wang, X.; Wu, G.; Yuan, W.; Yuan, T.; Zhu, B.; Liu, W.; Li, Z.; He, D.; Xue, Z.; Wang, Y.; Zheng, X.; Dong, J.; Chang, C.-R.; Chen, Y.; Hong, X.; Luo, J.; Wei, S.; Li, W.-X.; Strasser, P.; Wu, Y.; Li, Y. Engineering the Electronic Structure of Single Atom Ru Sites via

Compressive Strain Boosts Acidic Water Oxidation Electrocatalysis. *Nat. Catal.* **2019**, *2*, 304–313.

(70) Trasatti, S. Work Function, Electronegativity, and Electrochemical Behaviour of Metals. *J. Electroanal. Chem. Interfacial Electrochem.* **1972**, *39*, 163–184.

(71) Iwasita, T. Electrocatalysis of Methanol Oxidation. *Electrochim. Acta* **2002**, *47*, 3663–3674.

(72) Hodnik, N.; Bele, M.; Hočevar, S. New Pt-skin Electrocatalysts for Oxygen Reduction and Methanol Oxidation Reactions. *Electrochim. Commun.* **2012**, *23*, 125–128.

(73) Jovanovič, P.; Pavlišič, A.; Šelih, V. S.; Šala, M.; Hodnik, N.; Bele, M.; Hočevar, S.; Gabersček, M. New Insight into Platinum Dissolution from Nanoparticulate Platinum-Based Electrocatalysts Using Highly Sensitive In Situ Concentration Measurements. *ChemCatChem* **2014**, *6*, 449–453.

(74) Hodnik, N.; Cherevko, S. Spot the Difference at the Nanoscale: Identical Location Electron Microscopy in Electrocatalysis. *Current Opinion in Electrochemistry* **2019**, *15*, 73–82.

(75) Gatalo, M.; Moriau, L.; Petek, U.; Ruiz-Zepeda, F.; Šala, M.; Grom, M.; Galun, T.; Jovanovič, P.; Pavlišič, A.; Bele, M.; Hodnik, N.; Gabersček, M. CO-assisted Ex-situ Chemical Activation of Pt-Cu/C Oxygen Reduction Reaction Electrocatalyst. *Electrochim. Acta* **2019**, *306*, 377–386.

(76) Strasser, P.; Koh, S.; Anniyev, T.; Greeley, J.; More, K.; Yu, C.; Liu, Z.; Kaya, S.; Nordlund, D.; Ogasawara, H.; Toney, M. F.; Nilsson, A. Lattice-strain Control of the Activity in Dealloyed Core-shell Fuel Cell Catalysts. *Nat. Chem.* **2010**, *2*, 454–460.

(77) Stamenkovic, V. R.; Fowler, B.; Mun, B. S.; Wang, G.; Ross, P. N.; Lucas, C. A.; Markovic, N. M. Improved Oxygen Reduction Activity on Pt₃Ni(111) via Increased Surface Site Availability. *Science* **2007**, *315*, 493–497.

(78) Pavlišič, A.; Jovanovic, P.; Šelih, V. S.; Šala, M.; Bele, M.; Dražič, G.; Arcon, I.; Hočevar, S.; Kokalj, A.; Hodnik, N.; Gabersček, M. Atomically Resolved Dealloying of Structurally Ordered Pt Nanoalloy as an Oxygen Reduction Reaction Electrocatalyst. *ACS Catal.* **2016**, *6*, 5530–5534.

(79) Cherevko, S.; Zeradjanin, A. R.; Topalov, A. A.; Kulyk, N.; Katsounaros, I.; Mayrhofer, K. J. J. Dissolution of Noble Metals during Oxygen Evolution in Acidic Media. *ChemCatChem* **2014**, *6*, 2219–2223.

(80) Cherevko, S. Electrochemical Dissolution of Noble Metals Native Oxides. *J. Electroanal. Chem.* **2017**, *787*, 11–13.

(81) Hodnik, N.; Jovanovic, P.; Pavlišič, A.; Jozinovic, B.; Zorko, M.; Bele, M.; Šelih, V. S.; Šala, M.; Hočevar, S.; Gabersček, M. New Insights into Corrosion of Ruthenium and Ruthenium Oxide Nanoparticles in Acidic Media. *J. Phys. Chem. C* **2015**, *119*, 10140–10147.

(82) Jovanovic, P.; Hodnik, N.; Ruiz-Zepeda, F.; Arcon, I.; Jozinovic, B.; Zorko, M.; Bele, M.; Šala, M.; Šelih, V. S.; Hočevar, S.; Gabersček, M. Electrochemical Dissolution of Iridium and Iridium Oxide Particles in Acidic Media: Transmission Electron Microscopy, Electrochemical Flow Cell Coupled to Inductively Coupled Plasma Mass Spectrometry, and X-ray Absorption Study. *J. Am. Chem. Soc.* **2017**, *139*, 12837–12846.

(83) Strmcnik, D.; Uchimura, M.; Wang, C.; Subbaraman, R.; Danilovic, N.; van der Vliet, D.; Paulikas, A. P.; Stamenkovic, V. R.; Markovic, N. M. Improving the Hydrogen Oxidation Reaction Rate by Promotion of Hydroxyl Adsorption. *Nat. Chem.* **2013**, *5*, 300–306.

(84) Chen, S.; Kucernak, A. Electrocatalysis under Conditions of High Mass Transport Rate: Oxygen Reduction on Single Submicrometer-sized Pt Particles Supported on Carbon. *J. Phys. Chem. B* **2004**, *108*, 3262–3276.

(85) Chen, S.; Kucernak, A. Electrocatalysis under Conditions of High Mass Transport: Investigation of Hydrogen Oxidation on Single Submicron Pt Particles Supported on Carbon. *J. Phys. Chem. B* **2004**, *108*, 13984–13994.

(86) Gatalo, M.; Bele, M.; Ruiz-Zepeda, F.; Sest, E.; Šala, M.; Kamsek, A. R.; Maselj, N.; Galun, T.; Jovanovic, N.; Hodnik, N.; Gabersček, M. Double Passivation Water Based Galvanic Displace-

ment Method for Reproducible Gram Scale Production of High Performance Pt-alloy Electrocatalysts. *Angew. Chem.* **2019**, *131*, 13400–13404.

(87) Baldizzone, C.; Gan, L.; Hodnik, N.; Keeley, G. P.; Kostka, A.; Heggen, M.; Strasser, P.; Mayrhofer, K. J. J. Stability of Dealloyed Porous Pt/Ni Nanoparticles. *ACS Catal.* **2015**, *5*, 5000–5007.

(88) Li, Y.; Hart, J. L.; Taheri, M. L.; Snyder, J. D. Morphological Instability in Topologically Complex, Three-Dimensional Electrocatalytic Nanostructures. *ACS Catal.* **2017**, *7*, 7995–8005.

(89) Kasian, O.; Grote, J.-P.; Geiger, S.; Cherevko, S.; Mayrhofer, K. J. J. The Common Intermediates of Oxygen Evolution and Dissolution Reactions during Water Electrolysis on Iridium. *Angew. Chem., Int. Ed.* **2018**, *57*, 2488–2491.

(90) Topalov, A. A.; Katsounaros, I.; Auinger, M.; Cherevko, S.; Meier, J. C.; Klemm, S. O.; Mayrhofer, K. J. J. Dissolution of Platinum: Limits for the Deployment of Electrochemical Energy Conversion? *Angew. Chem., Int. Ed.* **2012**, *51*, 12613–12615.

(91) Hodnik, N.; Baldizzone, C.; Polymeros, G.; Geiger, S.; Grote, J.-P.; Cherevko, S.; Mingers, A.; Zeradjanin, A.; Mayrhofer, K. J. J. Platinum Recycling Going Green via Induced Surface Potential Alteration Enabling Fast and Efficient Dissolution. *Nat. Commun.* **2016**, *7*, 13164–13169.

(92) Gatalo, M.; Jovanovic, P.; Petek, U.; Šala, M.; Šelih, V. S.; Ruiz-Zepeda, F.; Bele, M.; Hodnik, N.; Gabersček, M. Comparison of Pt-Cu/C with Benchmark Pt-Co/C: Metal Dissolution and Their Surface Interactions. *ACS Appl. Energy Mater.* **2019**, *2*, 3131–3141.